Mon. Not. R. Astron. Soc. **332,** 367–382 (2002)

Temperature fluctuations in the intergalactic medium

Tom Theuns,[1]★ Saleem Zaroubi,[2] Tae-Sun Kim,[3] Panayiotis Tzanavaris[1] and Robert F. Carswell[1]

[1]*Institute of Astronomy, Madingley Road, Cambridge CB3 0HA*
[2]*Max-Planck Institut für Astrophysik, Postfach 123, 85740 Garching, Germany*
[3]*European Southern Observatory, Karl-Schwarzschild-Straße 2, D-85748 Garching bei München, Germany*

Accepted 2001 December 21. Received 2001 December 7; in original form 2001 September 21

ABSTRACT

The temperature of the low-density intergalactic medium (IGM) is set by the balance between adiabatic cooling resulting from the expansion of the Universe, and photoheating by the ultraviolet (UV) background. We have analysed the Lyα forest of 11 high-resolution quasar spectra using wavelets, and find strong evidence of a marked jump in the temperature at the mean density, T_0, of 60 ± 14 per cent over the redshift interval $z = [3.5, 3.1]$, which we attribute to reionization of He II. The jump can be seen in all three of our spectra that straddle redshift 3.3, at a significance of $\geqslant 99$ per cent. Below $z \sim 3.1$, our results are consistent with a smooth cooling down of the universe, as expected when adiabatic expansion dominates over photoheating by a UV background from quasi-stellar objects (QSOs) and galaxies. We find no evidence of thermal fluctuations on scales $\geqslant 5000\,\mathrm{km\,s^{-1}}$ larger than 50 per cent, which could be detected by our method, suggesting that the IGM follows a reasonably well-defined temperature–density relation. We demonstrate that the mean wavelet amplitude $\langle A \rangle \propto 1/T_0$, and calibrate the relation with hydrodynamical simulations. We find $T_0 \geqslant 1.2 \times 10^4\,\mathrm{K}$ at $z \geqslant 3.6$. Such high temperatures suggest that H I reionization occurred relatively recently.

Key words: hydrodynamics – intergalactic medium – quasars: absorption lines – cosmology: theory – large-scale structure of Universe.

1 INTRODUCTION

The intergalactic medium (IGM) can be observed in the spectra of distant objects such as quasars through resonant absorption in the Lyα transition of neutral hydrogen (Bahcall & Salpeter 1965; Gunn & Peterson 1965). The availability of high-resolution echelle spectrographs on large telescopes (HIRES on Keck and UVES on the Very Large Telescope) has provided us with data of unprecedented quality over recent years (see Rauch 1998 for a recent review). At the same time, a theoretical paradigm within the context of the cold dark matter (CDM) cosmology has emerged (e.g. Bi, Boerner & Chu 1992), well tested by numerical hydrodynamical simulations (Cen et al. 1994; Zhang, Anninos & Norman 1995; Miralda-Escudé et al. 1996; Hernquist et al. 1996; Wadsley & Bond 1996; Zhang et al. 1997; Theuns et al. 1998; Machacek et al. 2000), in which the absorption is produced by volume filling, photoionized gas, that contains most of the baryons at redshifts $z \sim 3$ (see e.g. Efstathiou, Schaye & Theuns 2000 for a recent review). The absorbers are locally overdense extended structures, close to local hydrostatic equilibrium (Schaye 2001). The combination of a predictive theory and superb data has led to a veritable revolution in IGM studies.

On large scales, the gas distribution is similar to that of the underlying dark matter, but on small scales pressure forces smooth the gas distribution, erasing most of the small-scale power. Combined with thermal broadening and peculiar velocities, this results in a strong suppression in the amplitude of the flux power spectrum on scales $\leqslant 200\,\mathrm{km\,s^{-1}}$ (e.g. Theuns, Schaye & Haehnelt 2000). Another consequence of the thermal content of the gas is a cut-off in the distribution of linewidths b below $\sim 20\,\mathrm{km\,s^{-1}}$ (Schaye et al. 1999), which is clearly present in observed line samples as well (e.g. Kirkman & Tytler 1997). Both these signatures can be used to infer the IGM temperature by calibrating the cut-off using simulations (Schaye et al. 1999, 2000; Ricotti, Gnedin & Shull 2000; Bryan & Machacek 2000; McDonald et al. 2001).

The IGM temperature can be used to constrain the reionization history because the thermal time-scales are long in the low-density gas probed by the Lyα absorption (Miralda-Escudé & Rees 1994). Consequently, the gas retains a memory of its heating *history*. At overdensities $\delta\rho/\langle\rho\rangle \leqslant 3$, shock heating and radiative cooling are unimportant and photoheating of the expanding gas introduces a tight density–temperature relation $T/T_0 = (\rho/\langle\rho\rangle)^{\gamma-1}$ (e.g. Hui &

★E-mail: tt@ast.cam.ac.uk

Gnedin 1997). A sudden epoch of reionization will make the gas nearly isothermal ($\gamma \sim 1$) at a temperature of $\sim 10^4$ K. Away from reionization, the density–temperature relation steepens again, asymptotically reaching $\gamma \sim 1.6$. The steepening occurs because denser gas has a higher neutral fraction, and hence a larger photoheating rate. If the heating rate can be computed reliably, given the observed sources of ionizing photons, then a measurement of the entropy of the gas can in principle determine the reionization epoch. If the sources responsible for reionizing hydrogen have a soft spectrum, there may be more than one reionization epoch as helium reionization requires harder photons.

There is some observational evidence that He II reionization occurs around $z \sim 3$, based on the occurrence of large fluctuations in the He II optical depth (Davidsen, Kriss & Wei 1996; Reimers et al. 1997; Heap et al. 2000), and the change in hardness of the ionizing spectrum as inferred from metal-line ratios (Songaila & Cowie 1996; Songaila 1998). The interpretation of the optical depth data is not straightforward, however (Miralda-Éscude, Haehnelt & Rees 2000), and there is some discussion in the literature about the reality and interpretation of the claimed change in metal-line ratios (Boksenberg, Sargent & Rauch 1998; Giroux & Shull 1997). Note that, if He II reionization does not occur instantaneously, various measures of the He II abundance change may well find a range of 'reionization epochs', given that they may sample different overdensities.

Reionization is not expected to be instantaneous because ionization fronts expand much faster into low-density voids than into the higher-density filaments (e.g. Gnedin 2000a). If the sources of ionizing photons are bright but scarce, then reionization will not be complete until the large ionized bubbles overlap. A consequence of such patchy reionization is that different regions might follow different ρ–T relations and so have different values of T_0. Such 'temperature fluctuations' may lead to apparent discrepancies between the different algorithms discussed earlier to measure T_0 and γ, as different methods may give other weights to regions in the same spectrum.

The aim of this paper is to test whether the data are consistent with a single, well-defined ρ–T relation and to investigate whether He II reionization can be detected by a jump in temperature. We use the wavelet analysis proposed by Theuns & Zaroubi (2000) and apply it to a set of high-resolution QSO spectra spanning a wide range of redshifts. We use hydrodynamical simulations to demonstrate that our method can detect variations in the amplitude T_0 of the temperature–density relation $\rho/\langle\rho\rangle \propto (T/T_0)^{\gamma-1}$ of the order of 50 per cent, even when these occur on scales as small as $\sim 5000\,\mathrm{km\,s^{-1}}$ ($1000\,\mathrm{km\,s^{-1}}$ corresponds to ~ 9.3 comoving Mpc h^{-1} and a redshift extent $\delta z = 1.33 \times 10^{-2}$ at redshift $z = 3$, in the currently popular flat, cosmological constant dominated model with matter density $\Omega_m = 0.3$.) The method presented here does not use simulations to identify regions of different temperatures. Recently, Zaldarriaga (2002) applied a similar analysis to QSO 1422+231 and showed that a model with two temperatures, which occupy comparable fractions of the spectrum, is constrained to have temperature variations smaller than a factor of 2.5.

This paper is organized as follows. Section 2 presents the data and Section 3 the simulations used to demonstrate the method. Section 4 describes the wavelet decomposition and the statistical tools making use of hydrodynamical simulations to illustrate the approach. Section 5 presents the results, and these are discussed in Section 6. Section 7 contains the summary. Readers not interested in the details of the method can skip directly to Section 4.3.1, which provides an illustration of the method for a simulated spectrum with imposed temperature fluctuations.

2 THE DATA

In our analysis, we have used data obtained with the high-resolution spectrograph on the Keck I telescope (Vogt et al. 1994), and UVES, the ultraviolet (UV) echelle spectrograph on the Very Large Telescope (VLT; Kueyen) (D'Odorico et al. 2000). We have combined line lists taken from the literature with publicly available spectra (Table 1), to obtain a set of 11 high-resolution quasi-stellar object (QSO) spectra that span a wide range of emission redshifts $z_{\rm em} = 1.7 \rightarrow 3.7$. High-resolution data is required because the lines are intrinsically narrow: $\sim 20\,\mathrm{km\,s^{-1}}$. The standard data reduction is described in the original references, with the exception of APM 0827+5255 which was reanalysed after calibration of the flux scale to remove echelle order mismatches (Tzanavaris & Carswell, in preparation). All spectra have signal-to-noise ratios of 40–50 per resolution element, and a similar resolution, $R \sim 40\,000$. Only two out of 11 of these spectra (QSOs APM 0827+5255 and 1422+293) were used in the analysis of the thermal evolution by Schaye et al. (2000).

Line profile fitting has been performed on the data. Voigt profiles are fitted to the absorption lines using a χ^2 minimization

Table 1. QSO spectra used.

QSO	$z_{\rm em}$	B^a	$\lambda\lambda$	$z_{\rm Ly\alpha}$	Comments	Ref.
HE0515−4414	1.719	14.9	3080–3270	1.53–1.69	VLT/UVES	1
J2233−606	2.238	17.5	3400–3890	1.80–2.20	VLT/UVES	1,2
HE1122−1648	2.400	17.7	3500–4091	1.88–2.37	VLT/UVES	2
HE2217−2818	2.413	16.0	3510–4100	1.89–2.37	VLT/UVES	1,2
Q0636+680	3.174	16.5	4300–4900	2.54–3.03	Keck/HIRES	3
Q0302−003	3.286	18.4	4808–5150	2.96–3.24	VLT/UVES	2
Q0956+122	3.301	17.8	4400–5000	2.62–3.11	Keck/HIRES	3
Q0014+813	3.384	16.5	4500–5100	2.70–3.20	Keck/HIRES	3
Q1422+231	3.620	16.5	3645–7306	2.91–3.60	Keck/HIRES	4
Q0055−269	3.655	17.9	4852–5598	2.99–3.60	VLT/UVES	2
APM08279+5255	3.911	15.2	4400–9250	3.20–3.72	Keck/HIRES	5

Note: ^{a}*B*-band magnitudes from the SIMBAD astronomical data base, except for QSO APM08279+5255, for which the *R*-band magnitude is from Irwin et al. (1998).
References: 1. Kim et al. (2001a); 2. Kim et al. (2001b); 3. Hu et al. (1995); 4. Rauch et al. (1997); 5. Ellison et al. (1999)

procedure, producing a list of lines with given column density, $N_{\rm H\,I}$ (cm^{-2}), width b (km s^{-1}) and absorption redshift z. Where possible, metal lines have been identified from line coincidences. This is in fact a crucial step, as such lines tend to be narrow and so might be mistaken for a cold Lyα cloud.

For QSOs Q0636+680, Q0956+122 and Q0014+813, we use the published line list given by Hu et al. (1995), who used their own automated line-fitting programme. All other spectra have been analysed with the semi-automatic line-fitting programme VPFIT[1] (Webb 1987; Carswell et al. 1987). The mock spectra from our simulations, described in the next section, are also fitted using VPFIT.

The line parameters from Voigt profile fitting are not unique (Kirkman & Tytler 1997). However, in the analysis described below, we never use the detailed properties of the lines, but rather analyse spectra as reconstructed from the line list. For QSO HE 1122−1648, we have redone our analysis using another line-fitting programme, FITLYMAN (Fontana & Ballester 1995), and the results are nearly identical.

3 HYDRODYNAMICAL SIMULATIONS AND MOCK SPECTRA

We use hydrodynamical simulations to illustrate the method described below. Briefly, these are simulations of a flat, vacuum-energy dominated cold dark matter model (matter density $\Omega_m = 0.3$, baryon fraction $\Omega_b h^2 = 0.019$, Hubble constant $H_0 = 100\,h\,{\rm km\,s^{-1}\,Mpc^{-1}}$, $h = 0.65$ and normalization $\sigma_8 = 0.9$). We have used CMBFAST (Seljak & Zaldarriaga 1996) to compute the appropriate linear transfer function.

The simulation code is based on HYDRA (Couchman, Thomas & Pearce 1995) and combines smoothed particle hydrodynamics (SPH, Gingold & Monaghan 1977; Lucy 1977) with adaptive P3M gravity (Couchman 1991). It has been modified extensively by one of us (TT) in order to be able to simulate the IGM. The code has been tested comprehensively, and has been parallellized in the OpenMP standard. Non-equilibrium radiative processes (cooling, photoionization heating by a UV background and Compton cooling off the cosmic microwave background radiation) are included with rates given as in Theuns et al. (1998). The evolution of the UV background is chosen to give the thermal evolution as determined by Schaye et al. (2000; the simulation is referred to there as the 'designer simulation'). In this simulation, H I and He I reionize at a redshift $z \sim 7$ by soft sources, whereas He II reionization is delayed to a redshift $z \sim 3.4$. The simulation box is $12.5\,h^{-1}$ comoving Mpc on a side (corresponding to $\approx 1400\,{\rm km\,s^{-1}}$ at redshift $z = 3$), and gas and dark matter are represented with 2×256^3 particles of masses 1.45 and $8.25 \times 10^6\,{\rm M}_\odot$, respectively. The resolution of this simulation is sufficient to resolve the various line-broadening mechanisms (Theuns et al. 1998), which is of course crucial for this type of analysis. At the same time, effects of missing large-scale power on the statistics analysed here, are not very important at sufficiently high redshifts $\geqslant 2$ (Theuns & Zaroubi 2000).

In order to study the effect of temperature fluctuations on the properties of the absorption lines produced, we impose specific temperature–density relations, $T/T_0 = (\rho/\langle\rho\rangle)^{\gamma-1}$, on our simulation outputs. We impose such a $T-\rho$ relation on all gas particles with $\rho \leqslant \langle\rho\rangle$ or $T(\rho) \leqslant 2T_0(\rho/\langle\rho\rangle)^{\gamma-1}$ and $\rho \leqslant 10\langle\rho\rangle$. Models C and H (for cold and hot, respectively) have $T_0 = 1.5 \times 10^4$ and 2.2×10^4 K, respectively, with the same slope, $\gamma = 5/3$. We have used these two models to make mock spectra of length $\sim 50\,000\,{\rm km\,s^{-1}}$, typical of observed Ly$\alpha$ spectra of redshift ~ 3 QSOs. (These combined spectra use sets of Voigt profiles pertaining to fits of spectra of individual sightlines through the simulation box. Each spectrum is fitted such that the maximum transmission occurs at the edges, by taking advantage of the fact that the individual chunks are periodic.) In order to make the comparison to data more realistic, we impose the observed mean absorption on the spectra. In addition, we also add noise and 'instrumental broadening' following the procedure described in detail in Theuns et al. (2000).

Table 2. Mock spectra used. (T_0,γ) refers to the imposed temperature–density relation, $V = 5 \times 10^5\,{\rm km\,s^{-1}}$ is the length of each spectrum.

Spectrum	(T_0,γ)
S1	$(1.5 \times 10^4, 5/3)$ for $v \leqslant 0.5V$ $(2.2 \times 10^4, 5/3)$ for $v \geqslant 0.5V$
S2	$(2.2 \times 10^4, 5/3)$ for $\lvert v - V/2\rvert \geqslant 2500$ $(1.5 \times 10^4, 5/3)$ else
S3	$(2.2 \times 10^4, 5/3)$[a]

[a]Mean flux $\bar{F} = 0.64$ (0.6) for $v \leqslant V/2$ ($v \geqslant V/2$).

Below we analyse several such mock spectra (Table 2). Spectrum S1 is composed of spectra drawn from model C for its first half, and from model H for its second half. Spectrum S2 is drawn from model H, except for a cold gap of length $5000\,{\rm km\,s^{-1}}$ drawn from model C in the middle of the spectrum. Finally, S3 is a single temperature model (H), but the mean absorption is scaled to be respectively 0.64 and 0.6 in the lower and upper-redshift halves of the spectrum, respectively.

To illustrate the effect of varying γ, we also compute spectra for models with imposed $T-\rho$ relations of $(T_0, \gamma) = (1.5 \times 10^4, 1)$ and $(2.2 \times 10^4, 1)$. (The neglect of extra broadening due to pressure effects and peculiar velocities in spectra with imposed equation of state artificially decreases the differences in line shapes for different T_0 models.) In addition to these simulations, we use another set of four simulations evolved with 2×64^3 particles in a box of size $2.5\,h^{-1}$ Mpc and the same ΛCDM cosmology as the others. These simulations have been run with different heating rates, to give them different values of $\log_{10}T_0 = [4.0, 4.1, 4.2, 4.3]$ but the same value of $\gamma \approx 1.4$. The mock spectra from these simulations are computed in the same way as the others.

These mock spectra are then scaled to have the same mean absorption as the data. We have used VPFIT to produce line lists for all mock spectra, and this allows us to treat data and simulation in an identical fashion for the wavelet analysis presented in the next section.

4 METHOD

4.1 Wavelet projection

A discrete wavelet is a localized function with a finite bandwidth (see e.g. Press et al. 1992 for an introduction and original references to the application of wavelets to a wide variety of problems). This makes wavelets useful for characterizing linewidths in a spectrum, as the amplitude of the wavelet will be related to the width of the line, and the position of the wavelet to

[1] For details on VPFIT, see http://www.ast.cam.ac.uk/ ~ rfc/vpfit.html

the position of the line. Pando & Fang (1996) used a wavelet analysis to describe clustering of Lyα absorption lines. Theuns & Zaroubi (2000) used the Daubechies 20 wavelet (Daubechies 1988) to characterize temperature fluctuations in a Lyα spectrum. Independently, Meiksin (2000) used the same wavelet basis to show that most of the information in a spectrum is carried by a small fraction of the wavelets. More recently, Jamkhedar, Bi & Fang (2001) used a multi-scale analysis based on wavelets to better describe the transmission power spectrum taking into account uncertainties in the applied continuum.

Discrete wavelets are also a set of orthogonal basis functions. Consequently, we can borrow notation from quantum mechanics to write any function $|\psi\rangle$ as a sum over its wavelet projections, $|\psi\rangle = \sum_n \langle\psi_n|\psi\rangle|\psi_n\rangle$. Here, $|\psi_n\rangle$ is the wavelet function of level n, $\langle\psi_n|\psi\rangle$ the projection of $|\psi\rangle$ on to $|\psi_n\rangle$, and n the 'quantum number' of the basis function. Characteristic for wavelets is that they have a finite extent in both the spatial direction, and the frequency domain, i.e. they are like a wave-packet instead of a single momentum wave. So we'll need two indices to denote a given wavelet basis function, $|\psi_{n,p}\rangle$, where n denotes the characteristic frequency ('width'), and p the position of the wavelet.

In this paper we will investigate the properties of the spectrum in terms of a given single *frequency* of the wavelet, i.e. we will study

$$|\psi(n)\rangle \equiv \sum_p \langle\psi_{n,p}|\psi\rangle|\psi_{n,p}\rangle. \quad (1)$$

Note that summing $|\psi(n)\rangle$ over n will give back the original function $|\psi\rangle$. We are left to tune the frequency n to make it most sensitive to the temperature. We have chosen to use the Daubechies 20 wavelet, as in Theuns & Zaroubi (2000), who give examples of the decomposition of a spectrum in terms of that wavelet. Note that computing the wavelet projection equation (1) is computationally very similar to performing a fast Fourier transform, and many standard computer packages have wavelet transforms built in. The usage of wavelets is not very common in astronomy; we would therefore like to note that the computation of the projection equation (1) requires a handful of programming lines in standard software packages such as IDL, and much less than 1 s of computer time to evaluate. For a given choice of the wavelet, the decomposition in equation (1) is unique.

Theuns & Zaroubi (2000) showed that the projection in equation (1) is already very sensitive to the temperature of the gas, because narrow lines tend to generate larger wavelet coefficients than broader lines, for a suitable choice of n. Here we describe four improvements to that method.

(i) Because the $|\psi_{n,p}\rangle$ are orthogonal basis functions, they change sign at least once, in contrast to an absorption spectrum. In particular, the Daubechies 20 wavelet does not look like an absorption line at all, but is more similar to its *derivative*. So we found it advantageous to project the scaled *derivative* of the spectrum $F(\lambda)$ with respect to velocity $v, \partial F/\partial v (F+\eta)^{-1}$. Here, the 'velocity' v is defined as a function of wavelength λ through $\mathrm{d}\lambda/\lambda = \mathrm{d}v/c$, where c is the speed of light, and the parameter $\eta = 0.2$ is introduced to avoid division by zero close to the zero level.

(ii) The positional localization of the narrow wavelet (width $\sim 15\,\mathrm{km\,s^{-1}}$) that we will use below is far better than what we require to determine a jump in temperature. We take advantage of this to improve the frequency resolution – and hence the sensitivity to small changes in the linewidths – of the wavelet projection at the expense of its localization by computing

$$|\psi(n,\delta)\rangle \equiv \sum_p \max_{(-1/2,0,1/2)\times\delta}(|\langle\psi(n,p)|\psi(-\delta)\rangle \times |\psi(n,p+\delta)\rangle|). \quad (2)$$

Thus we shift the input function by δ to the left, $|\psi(-\delta)\rangle$, project it on to the wavelet, and shift the result by the same δ to the right. We do this for $\delta = -1/2, 0, 1/2$ times the width of the wavelet, and at each position take the maximum absolute value of the three projections and denote the result by $|\psi(n,\delta)\rangle$. This step is not crucial to the method, but does improve its sensitivity in finding temperature fluctuations imposed in the mock spectra.

(iii) Observed spectra contain metal lines in addition to Lyα lines. As described in the data section, we use VPFIT to fit Voigt profiles, $V(b_i, N_i, \lambda_i)$, to the spectrum. Here, $V(b_i, N_i, \lambda_i, X_i)$ denotes a Voigt profile of species X_i with column density N_i, width b_i and centred on λ_i. Using this decomposition, we can reconstruct an (almost) 'metal free' spectrum,

$$F_{\mathrm{VP}} = \exp\left[-\sum_i V(b_i, N_i, \lambda_i, \mathrm{Ly}\alpha)\right]. \quad (3)$$

(Note that we still impose instrumental broadening on this reconstruction.)

The decomposition equation (2) is very good at identifying very narrow lines $\leqslant 15\,\mathrm{km\,s^{-1}}$. When applying the method to data, it is sometimes impossible to decide whether such a narrow line is a metal line or not, because the corresponding other metal transitions may not fall in the observed region of the spectrum, or fall on top of a strong Lyα line. In cases where a strong wavelet signal results from a single Voigt profile, we have decided to flag the line as a potential metal line, and not consider it any further in the rest of the analysis. Typically, only a handful of lines (out of several hundreds) are removed per spectrum. This is of course a somewhat subjective procedure, but is unlikely to introduce any *positive* detection of a spurious correlation signal.

Using F_{VP} instead of the original spectrum F has the added benefit that it is also noise free, making it easier to take the derivative (step 1), and will also be extremely useful in the statistical analysis. The decomposition in Voigt profiles is not unique, but as we only use the reconstructed spectrum and not the detailed properties of the fitted lines, we expect the spectrum F_{VP} to be nearly independent of the actual manner in which Voigt profiles were fitted. In particular, we were unable to detect any systematic differences in line shapes between the original spectrum and the reconstruction, using either our mock spectra or observed data. We also redid the analysis for one QSO spectrum (QSO HE 1122–1648) using FITLYMAN (Fontana & Ballester 1995), another line-fitting programme, and found the same results.

In the absence of evolution in the b parameters, linewidths $\Delta\lambda$ will increase with redshift $\propto(1+z)$. This pure 'expansion' effect can be compensated for by rebinning the spectrum to velocity space, and VPFIT performs such a rebinning.

(iv) The spectrum also contains strong lines. Their square shape tends to generate large wavelet amplitudes, an effect similar to the Gibbs phenomenon familiar from Fourier analysis. In addition, in the saturated region of the strong lines, the wavelet amplitude becomes zero. These fluctuations in the wavelet amplitudes do not contain any information on the IGM temperature and so we ignore them. We begin by identifying all regions of the spectrum within 1 per cent of being black. All pixels within 1.5 times the

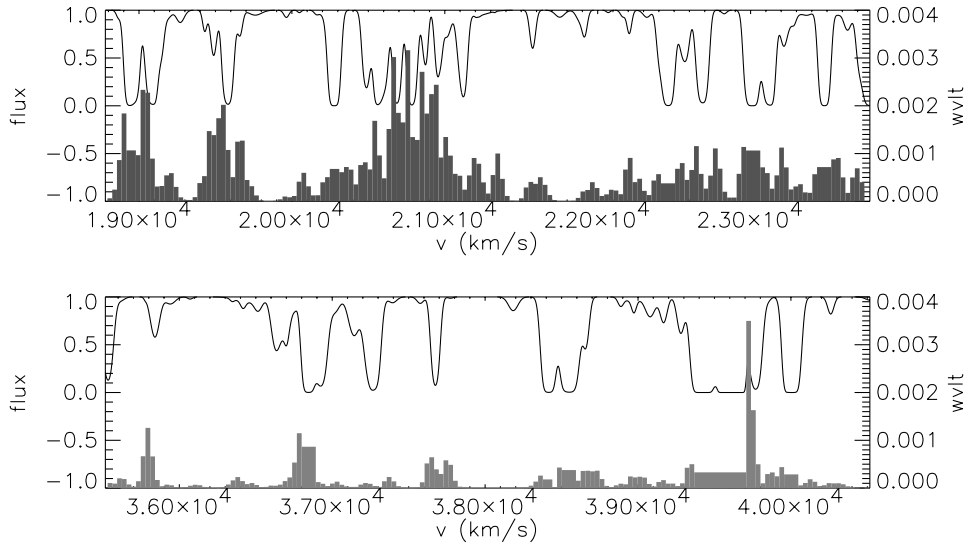

Figure 1. Flux (lines, left-hand scale) and wavelet amplitude averaged over 100 km s^{-1} (filled histogram, right-hand scale) for a stretch of spectrum of length 5000 km s^{-1} from simulation C ($T_0 = 1.5 \times 10^4$ K, top panel) and the hotter simulation H ($T_0 = 2.2 \times 10^4$ K, bottom panel). The wavelet amplitudes tend to be significantly larger in the colder model.

wavelet-width of such a region are ignored in the statistical analysis described in the next section.

In summary: we start by fitting the original spectrum $F(\lambda)$ with Voigt profiles, and reconstruct the spectrum from the fit, using only those lines not identified as (or suspected to be) metal lines. For this spectrum, $F_{\rm VP}(v)$, we compute the wavelet projection of its normalized derivative, $F_{\rm VP}(\delta) = \sum_p \max_{(-1/2,0,1/2)\times\delta}(|\langle\psi(n,p)| \partial F_{\rm VP}/\partial v(F_{\rm VP}+0.2)^{-1}(-\delta)\rangle|\psi(n,p+\delta)\rangle|)$. We use the correlations in $F_{\rm VP}(\delta)$ to quantify temperature variations along the spectrum. Fig. 1 illustrates the procedure. It shows two stretches taken from spectrum S1 of length 5000 km s^{-1}, corresponding to model C and the 50 per cent hotter model H, respectively. The wavelet amplitudes tend to be significantly larger in the spectrum taken from the colder model. The wavelet amplitudes can therefore serve as a thermometer.

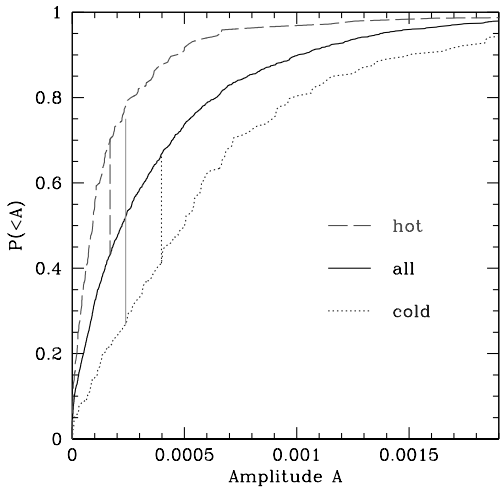

Figure 2. Cumulative distribution of wavelet amplitudes for spectrum S1 (full line labelled all), its hot half (long dashed line) and its cold half (dotted line). Vertical lines indicate the maximum differences between the cumulative distributions.

4.2 Statistical analysis

4.2.1 Cumulative distribution of wavelet coefficients

In the previous section we illustrated the strong dependence of the wavelet amplitude on the temperature of the gas – cooler gas generates a larger fraction of narrow lines with correspondingly higher wavelet amplitudes A, on average. Thus we can now recognize temperature fluctuations by identifying regions over which the wavelet amplitudes are unusually large (a cold region), or unusually small (a hot region). We will quantify the extent to which the wavelet amplitudes in two regions of the spectrum differ, by $\Delta(v_1, \partial v_1; v_2, \partial v_2)$, the maximum difference between the two cumulative distributions of A in the regions $[v_1, v_1 + \partial v_1]$ and $[v_2, v_2 + \partial v_2]$ (velocities v are in km s^{-1}). [Note that $\Delta(v_1, \partial v_1; v_2, \partial v_2) = -\Delta(v_2, \partial v_2; v_1, \partial v_1)$.] We will denote this difference as $\Delta(v,\partial v)$ when one of the windows refers to the whole spectrum.

The cumulative distribution $P(\leqslant A)$ of the wavelet amplitude A for the two windows shown earlier in Fig. 1 ($[1.9 \times 10^4, 5 \times 10^3]$ and $[3.55 \times 10^4, 5 \times 10^3]$, respectively) is plotted in Fig. 2, together with the cumulative distribution of A over the whole spectrum of S1. The three distributions appear to be quite different, as expected. The differences Δ between the cumulative distributions are shown as vertical lines. Note that Theuns & Zaroubi (2000) also used $P(\leqslant A)$ to characterize the $T-\rho$ relation.

The quantity $\Delta(v,\partial v)$ can be used as a (uncalibrated as of yet) thermometer. In Fig. 3 we plot $\Delta(v, 5 \times 10^3)$ as a function of the starting position v of the window for the simulated spectrum S1. Notice that as long as v is in the first half of the spectrum – in which case the window is drawn from the cold simulation C – then $\Delta \sim -0.2$. There is a sudden transition around $v \sim 2.5 \times 10^4$ km s^{-1} where Δ jumps to values $\sim +0.2$, as the window starts to fall in the stretch of spectrum drawn from the hotter model H. We want to stress again that, for a given wavelet basis, $\Delta(v, 5 \times 10^3)$ follows uniquely from projecting the spectrum on a set of basis functions.

Our aim is now to use $\Delta(v_1, \partial v_1; v_2, \partial v_2)$ to find regions with different temperatures, and use $\Delta(v,\partial v)$ as a measure of T_0.

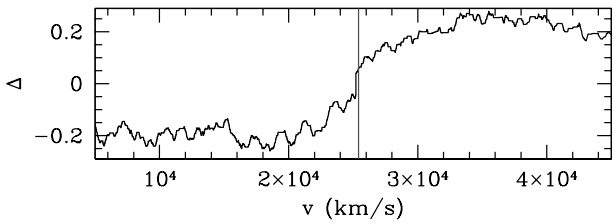

Figure 3. Maximum difference Δ between the cumulative distribution of A in a window of size $5000\,\mathrm{km\,s^{-1}}$ starting at velocity v, and the cumulative distribution of A over the whole spectrum, for the simulated spectrum S1. Negative values of Δ indicate regions where the window has a larger fraction of high wavelet amplitudes than the spectrum as a whole. $\Delta \sim -0.2$ for the first half of the spectrum, and $\sim +0.2$ for the second half, showing that Δ is able to recognize that the first half of spectrum S1 is cold, and the second half is hot.

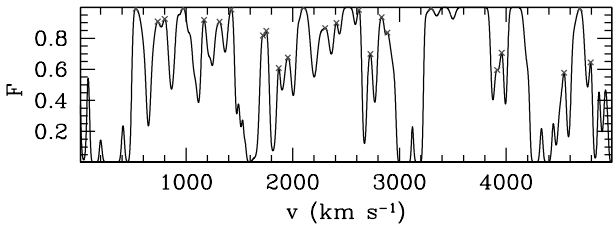

Figure 4. Stretch of spectrum of QSO 1422+231. A piece of spectrum between two crosses is identified as an 'absorption feature' in the randomization procedure. Voigt profile fitted absorption lines with central wavelengths that fall within the same absorption feature always keep their relative spacing when randomizing the spectrum, thereby keeping the detailed line shape identical between original and randomized spectrum.

However, how can one judge whether a given value of Δ is *statistically* significant? The usual way (Kolmogorov–Smirnov test) to decide whether two data sets are drawn from the same underlying distribution is to evaluate a particular function of both $|\Delta|$, and of the effective number of degrees of freedom N. Unfortunately, in the present case it is unclear how to determine N, as pixels are correlated. One way to make progress is to use randomized spectra, in which any temperature fluctuations have been destroyed in the randomization procedure, to *calibrate* the distribution of Δ and hence determine how statistically significant the difference seen in Fig. 2 is. Note that, if a randomized spectrum by chance produces a peculiar value of Δ, it is not due to temperature fluctuations, as the temperature–density relation is not different from that of the rest of the spectrum. The full procedure to assign a statistical significance to unusual regions is described next.

4.2.2 *Randomized spectra*

The aim of this procedure is to produce new spectra from the data, in which the absorption lines have the same shapes, but any *correlation* between the lines is destroyed. One could in principle randomize the positions of the Voigt profiles in equation (3), but the resulting spectra turn out to be quite different from the original one. The reason is that many absorption features are composed of several Voigt profiles (often with large error estimates for the fitted parameters), some of which may be quite narrow and are introduced to obtain a good fit. When randomizing Voigt profiles, such a narrow line will tend to occur on its own, and this causes clear systematic differences between the randomized spectra and the original one.

We have chosen instead to randomize the positions of the absorption features ('absorption lines' as opposed to Voigt profiles, in what follows) themselves. An absorption line is defined as a stretch of spectrum between two local maxima in F_{VP}. Voigt profiles are now assigned to a line, if the centre of the profile falls between the two maxima that define the line. Randomized spectra are then obtained from randomizing the positions of the *lines*, making sure that lines do not overlap (but the Voigt profiles may), resampling them with replacement. In the tests presented below, we will show that these randomized spectra are not distinguishable from the original one, in the *absence* of imposed temperature fluctuations.

An example of the identification of lines for part of the spectrum of QSO 1422+231 is shown in Fig. 4, where local maxima are indicated by crosses. We use only those local maxima where the flux $F \geqslant 0.5$. A histogram of the widths of the lines is shown for reference in Fig. 5. The typical widths of the lines is $\sim 100\,\mathrm{km\,s^{-1}}$, with a tail to larger values.

Given these randomized spectra, we can compute the probability distribution $P(\Delta)$, by randomly sampling $\sim 2 \times 10^4$ window pairs for each spectrum. The result is plotted in Fig. 6 (dotted line). Superposed is $P(\Delta)$ for the original spectrum S1, for window pairs

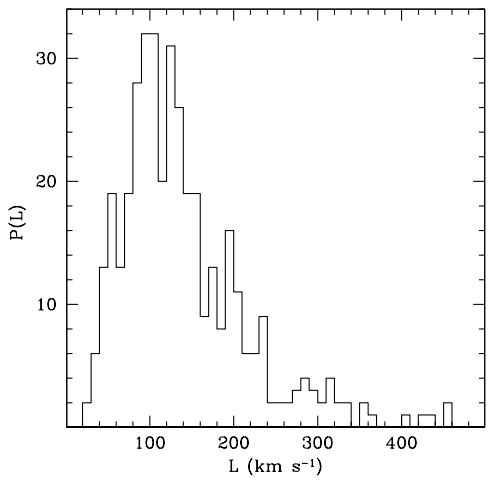

Figure 5. Histogram of the lengths of absorption features identified in QSO 1422+231.

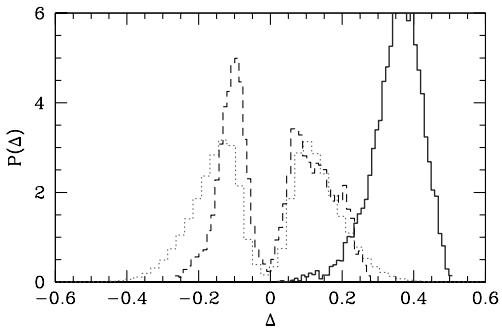

Figure 6. Probability distribution $P(\Delta)$ for windows of size $5000\,\mathrm{km\,s^{-1}}$ for windows drawn from 200 randomized spectra of spectrum S1 (dotted line). The dashed line refers to $P(\Delta)$ for the original spectrum S1, but only includes window pairs that fall in the same half of S1; the thick full line refers to window pairs that fall in different halves. The dotted and dashed histograms are very similar, because both refer to single-temperature models. The histogram referring to different temperature window pairs (full line) differs significantly from the case where both windows refer to the same temperature. This type of statistic is therefore useful in recognizing regions with different temperatures.

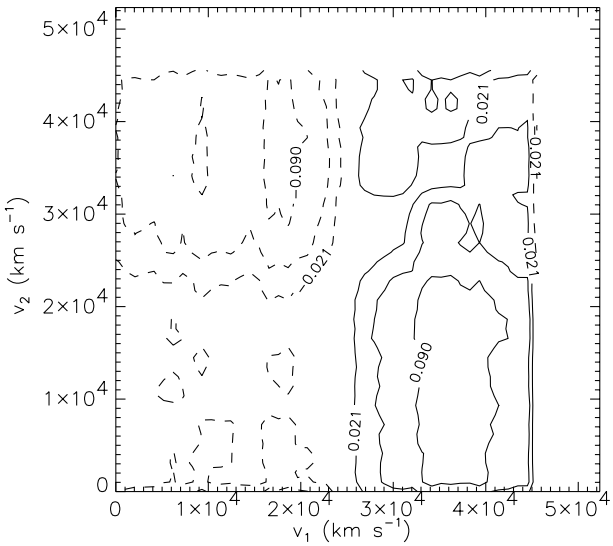

Figure 7. Contour plot for the correlation field $\mathcal{Q}$ for spectrum S1. Contours are drawn at levels 0.02, 0.05 and 0.09 for positive values (full lines) and negative values (dashed lines). The window size $\partial v = 5000\,\mathrm{km\,s^{-1}}$. The contour level -0.021 delineates the cold region, and level 0.021 delineates the hot region.

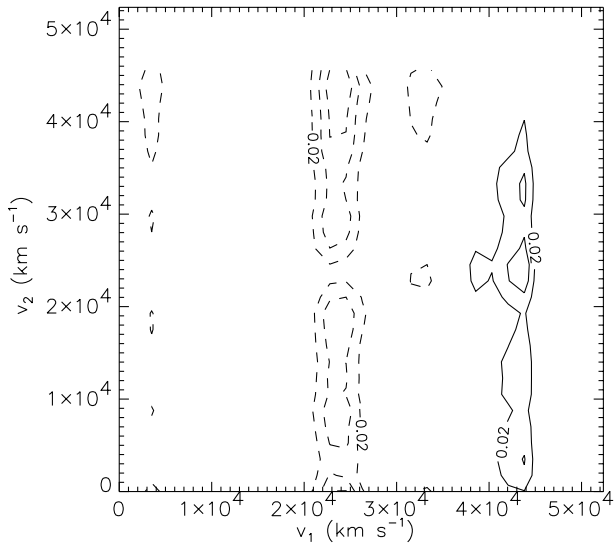

Figure 8. Same as Fig. 7 for spectrum S2. The cold gap in the middle of the spectrum stands out.

drawn from the same half of the spectrum (dashed line) and from different halves (full line). The randomized spectra have a similar $P(\Delta)$ as the original spectrum S1, when both windows are drawn from a single temperature region, but the mixed temperature $P(\Delta)$ (full line) is very different. The probability distribution $P(\Delta)$ from the randomized spectra allows us to assign a statistical significance to a given value of Δ.

4.2.3 Cluster analysis

In the previous sections we demonstrated how the difference Δ can be used as a thermometer, and how the statistics of $P(\Delta)$ can be used to decide whether a difference in temperature between two windows is statistically significant. Here we will combine these two results to identify regions in the spectrum that have a statistically significant different temperature as compared to the rest of the spectrum.

In order to do so, we study correlations in the field

$$\mathcal{Q}(v_1, v_2; \partial v) = \Delta(v_1, \partial v)|\Delta(v_1, \partial v; v_2, \partial v)|. \quad (4)$$

Recall that large values of $|\Delta(v_1, \partial v; v_2, \partial v)|$ suggest different temperatures between the two windows $[v_1, v_1 + \partial v]$ versus $[v_2, v_2 + \partial v]$. Because we multiply this quantity with $\Delta(v_1,\partial v)$ to obtain $\mathcal{Q}$, we can also judge whether window $[v_1, v_1 + \partial v]$ is cold or hot (in which case $\mathcal{Q} \ll 0$ and $\mathcal{Q} \gg 0$, respectively), as we demonstrated in Fig. 3.

A contour representation of $\mathcal{Q}$ is plotted in Fig. 7 for spectrum S1, which shows that $\mathcal{Q} < 0$ in the top left-hand corner, and $\mathcal{Q} > 0$ in the bottom right-hand corner. Recalling our previous results, this indicates that the first half of the spectrum is cold, and has a significantly different temperature from the second half, which consequently is hot. Recall that this is indeed the case for our simulated spectrum S1.

The next step is to determine the extent of the region where the temperature differs significantly from the rest of the spectrum. We do this using a cluster analysis as follows. Given the normalized probability distribution $P(\Delta)$, determined from randomized spectra without fluctuations, we determine Δ_f such that $\int_{-\infty}^{\Delta_f} P(\Delta)\,\mathrm{d}\Delta = f$, for $f = 0.1$ and $f = 0.9$. That is, only 10 per cent of window pairs have $\Delta \leqslant \Delta_{0.1}$, and equally 10 per cent of pairs have $\Delta \geqslant \Delta_{0.9}$. We define $\mathcal{Q}_l \equiv |\Delta_{0.1}\Delta_{0.9}|$ as a good first indicator of whether a window has a peculiar temperature, by comparing $\mathcal{Q}$ with $\mathcal{Q}_l$. Windows with $\mathcal{Q} < -\mathcal{Q}_l$ are likely to be peculiarly cold, those with $\mathcal{Q} > \mathcal{Q}_l$ peculiarly hot. In Fig. 7, the lowest contour level shown is $\mathcal{Q}_l$, and indeed, these contour levels delineate the low (cold) and high (hot) regions of the spectrum.

Another example of the field $\mathcal{Q}$, now for the spectrum S2, is shown in Fig. 8. Recall that S2 has a single cold region located in $[2.2 \times 10^4, 2.7 \times 10^4]$. This peculiar region falls below the contour level $-\mathcal{Q}_l$ and is therefore neatly detected by the procedure described so far. Note that there are other, smaller, regions where $|\mathcal{Q}| \geqslant \mathcal{Q}_l$ in this example.

We now define a *cluster* as a connected region where $|\mathcal{Q}| \geqslant \mathcal{Q}_l$. In practise, we identify clusters by interpolating $\mathcal{Q}$ on to a grid of grid size $\partial v/5$ using cloud-in-cell interpolation. A cluster is then a set of connected grid cells,[2] which each have $|\mathcal{Q}| \geqslant \mathcal{Q}_l$. The *weight* of a cluster is the integral of $\mathcal{Q}$ over its cells. The motivation for doing this is that a region of unusual temperature will have a large extent in a plot such as Fig. 7, and so will have a large weight. We will use the randomized spectra to judge the statistical significantly of those weights.

When identifying clusters, we impose 'periodic boundary conditions' in the vertical direction (i.e. cells at the upper and lower extreme, but the same horizontal position v_1, are also neighbouring cells). This may seem strange at first, but consider the cluster identified in Fig. 8. Without periodic boundary conditions, there would be two clusters (of roughly half the size) above the cold region $[2.2 \times 10^4, 2.7 \times 10^4]$. The reason that these two clusters are not connected but appear to have a hole around $v_2 \sim 2.5 \times 10^4$ is of course because $v_1 \sim v_2$ there, and both windows refer to the *same* stretch of spectrum – hence $\mathcal{Q} \sim 0$. So clearly that region of the plane *is not* peculiar as it does not refer to windows of different temperatures. However, if the cold region had been closer to the

[2] Grid cells that neighbour each other, either horizontally or vertically, are called 'connected'.

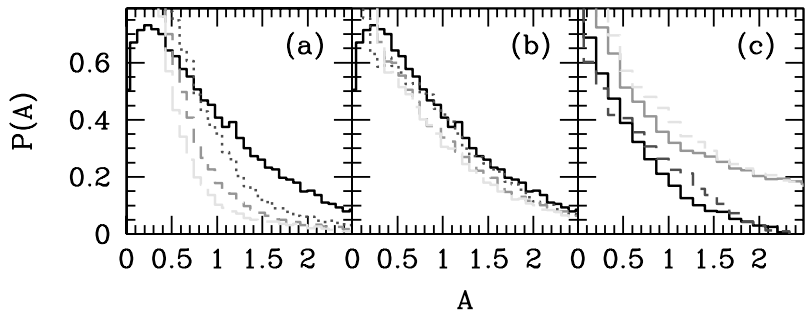

Figure 9. Dependence of the probability distribution $P(A)$ of wavelet amplitudes on T_0 and γ. Panel (a): $P(A/\langle A_1\rangle)$ versus $A/\langle A_1\rangle$ for models with $\log_{10}T_0 = [4.0, 4.1, 4.2, 4.3]$ (full, dotted, short-dashed and long-dashed lines, respectively) and $\gamma = 1.4$. The amplitudes have been scaled by the mean wavelet amplitude $\langle A_1\rangle$ of the coldest model. In panel (b), the distribution $P(A/\langle A\rangle)$ is scaled using the mean of the distribution. In panel (c) we show the normalized distributions $P(A/\langle A\rangle)$ for models with $(\log_{10}T_0, \gamma) = (4.18, 1)$ and (4.18,5/3) (lower curves, full and dashed line, respectively, offset vertically by -0.1) and $(\log_{10}T_0, \gamma) = (4.34, 1)$ and $(4.34, 5/3)$ (full and dashed lines, respectively, offset vertically by 0.1). Panel (a) shows that $P(A)$ depends on T_0, with hotter models having a smaller fraction of large wavelet amplitudes, as expected. Panel (b) demonstrates that the difference in shape is mostly due to the difference in mean $\langle A\rangle$ of the distribution. Finally, panel (c) shows that γ has an effect on the shape of $P(A/\langle A\rangle)$ as well, such that models with a larger γ are larger around the mean of the distribution.

start, or the end of the spectrum, there wouldn't have been a hole, and hence the cluster would have been identified with nearly twice the weight it has now. This is clearly not what we want. Imposing periodic boundary conditions connects these two clusters into one again. In this case, the weight of the cluster does *not* depend on its position. Note that clusters that correspond to low temperatures have a negative weight.

After cluster identification, we can introduce the new field, $\mathcal{C}$, defined on the grid, where $\mathcal{C}(v_1, v_2) = 0$ if the cell does not fall into a cluster, and equals the weight of the cluster if it does. Finally, we project $\mathcal{C}$ on to the spectrum,

$$C_P(v_1) = \sum_{v_2} \mathcal{C}(v_1, v_2). \tag{5}$$

For a given velocity, $C_P(v)$ is a measure of the fraction of spectrum that has a significantly different temperature. The level of significance of a given value $C_P(v)$ is obtained by performing the same analysis on all the randomized spectra, from which we can compute the probability distribution $P(C_P)$. This concludes the description of the statistical analysis.

4.3 Temperature calibration

The method described so far identifies regions of significantly different temperatures. We can get an idea of how much the temperatures differ by examining in more detail the probability distribution $P(A)$ of wavelet amplitudes. The shape of this distribution depends mainly on its average $\langle A\rangle$, as pointed out by Zaldarriaga (2002), and demonstrated in Fig. 9. There is an additional dependence on the slope γ of the $T-\rho$ relation, in that models with larger γ have a higher fraction of wavelets around the mean.

In turn, $\langle A\rangle$ correlates strongly with the temperature $T_\delta \equiv T\delta^{\gamma-1}$ of the gas, at some overdensity $\delta \equiv \rho/\langle\rho\rangle$. For the mean absorption appropriate for $z = 3$, $\delta \approx 1.2$. Fig. 10 shows that $T_\delta \propto \langle A\rangle^{-1}$, for simulated models with a range of values for T_0 and γ. So without calibrating the $\langle A\rangle - T$ relation with simulations, one can still estimate temperature ratios. If one is willing to normalize the relation using simulations, then it is possible to measure $T_{1.2}$ directly.

In the linear regime, the baryonic overdensity $\delta_{\rm IGM}$ is smoothed with respect to the dark matter field $\delta_{\rm DM}$ according to $\delta_{\rm IGM}(k) \propto \delta_{\rm DM}(k)/k^2T$, at high wavenumbers k (e.g. Bi & Davidsen 1997). The wavelet amplitude $\langle A\rangle$ is a measure of the rms of $\delta_{\rm IGM}$ on small scales, which explains the scaling $\langle A\rangle \propto \langle\delta^2_{\rm IGM}\rangle^{1/2} \propto T^{-1}$.

The mean $\langle A\rangle$ can be directly computed for a given spectrum, and the linear relation of Fig. 10 can then be used to estimate $T_{1.2}$. In the simulations we measured a variation of ~ 30 per cent in $\langle A\rangle$ over regions of $\partial v = 5000\,{\rm km\,s^{-1}}$, in single temperature models. The corresponding error bars are indicated in Fig. 10. When applying this linear scaling to data of velocity extent ∂v, we will also assume a similar error $\sim 30(\partial v/5000\,{\rm km\,s^{-1}})^{-1/2}$ per cent. The values $\gamma = 1$ and $\gamma = 5/3$ are likely to span the range encountered when applying this calibration to real data.

4.3.1 *Summary and illustration*

The method we have devised consists of three steps.

(i) Compute the contribution of a narrow wavelet to the derivative of the spectrum. We used simulation to show that the amplitude A of such a wavelet anticorrelates strongly with the temperature of absorbing gas (Fig. 1). The cumulative distribution $P(<A)$ can be used to characterize the $\rho-T$ relation. For example, we used the maximum distance Δ between the cumulative distributions of two stretches of spectrum to judge which stretch corresponds to higher temperatures (Fig. 3).

(ii) Generate random spectra from the original data by scrambling the line list. These random spectra are used to compute the probability distribution $P(\Delta)$ for spectra *without* temperature fluctuations.

(iii) Identify unusual regions in the spectrum that correspond to large values of $|\mathcal{Q}|$, where $\mathcal{Q}(v_1, v_2, \partial v)$ is defined in equation (4). Use a clustering analysis to better characterize the size of these regions. Project the resulting clusters on to the spectrum to obtain $C_P(v)$ (equation 5) and use the randomized spectra to associate the statistical significance.

An estimate of the temperature ratio of different regions can be obtained by comparing the mean wavelet amplitudes and using the relation $T \propto \langle A\rangle^{-1}$.

The final result of applying the above procedure to the simulated spectra S1, S2 and S3 is shown in Fig. 11. For each value of $C_P(v)$, we find the fraction f of random spectra that have a comparable

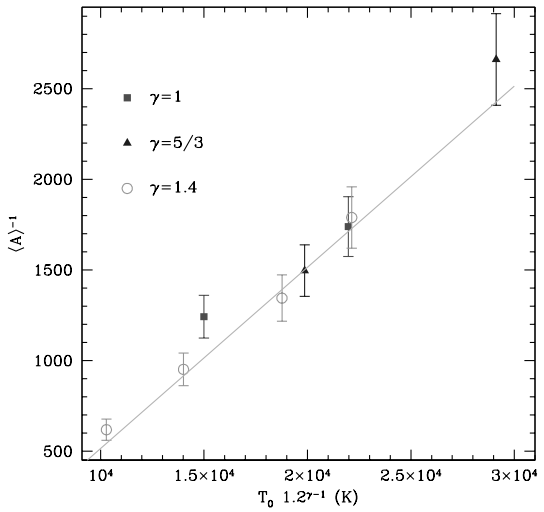

Figure 10. Temperature $T_{1.2} \equiv T_0 1.2^{\gamma-1}$ at an overdensity of 1.2, versus the inverse $\langle A\rangle^{-1}$ of the wavelet amplitude for models with different values of T_0 and γ at a redshift $z = 3$. The values of γ are indicated in the panel. The error bars assume 30 per cent uncertainty on $\langle A\rangle$ per 5000 km s^{-1}. The line is a least-squares fit to the points, demonstrating the scaling $T_{1.2} \propto \langle A\rangle^{-1}$.

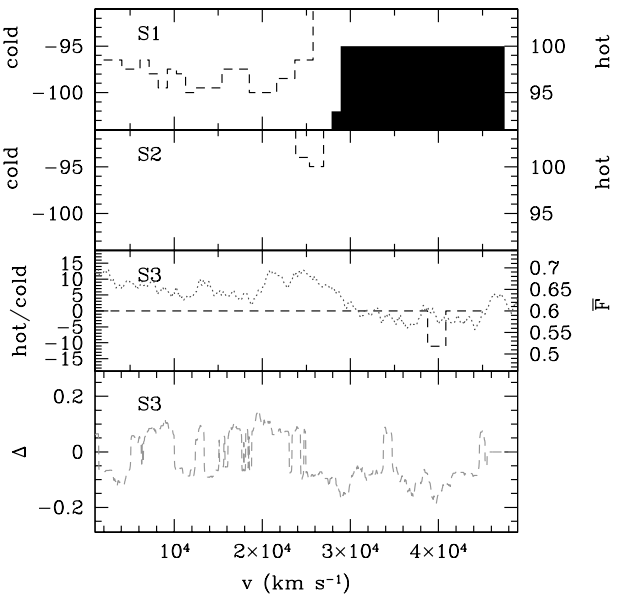

Figure 11. Statistical significance that the temperature in a window of size 5000 km s^{-1} starting at velocity v differs from the spectrum as a whole. The outlined histogram (left-hand scale) is significance in per cent for cold regions, the filled histogram (right-hand scale) for hot regions. The dotted line (right-hand scale) denotes the flux, smoothed over 5000 km s^{-1}. Both the hot and cold regions in S1 (top panel) are assigned a significance of 100 per cent. The cold gap in spectrum S2 has a significance of 95 per cent. Finally, no significant region is detected in the single temperature spectrum S3 (bottom panel). The bottom panel shows the Δ statistic for S3, which can be compared with the corresponding curve for S1 in Fig. 3.

cluster, and plot the significance $100(1.-f)$ in per cent [or $100(f-1.)$ for cold regions], both for hot regions (filled histogram, right-hand scale) and for cold regions (histogram, left-hand scale). The hot and cold regions in spectrum S1 both have a significance of $\sim$100 per cent, meaning that none of the (200 in this case) randomized spectra contain clusters that large. The cold gap in spectrum S2 is significant at the 95 per cent level.

The different ρ–T relations in the spectra S1 and S2 were imposed on the simulations in post processing. This is likely to underestimate the differences in linewidths, compared to models in which the temperature is different *during* the simulation as well. For example, Theuns et al. (2000) showed that linewidths for simulations with identical *imposed* ρ–T relations are measurably different if the underlying simulations had different temperatures. The reason is that simulations with different temperatures vary in the amount of Jeans smoothing and pressure-induced peculiar velocities, which also contribute to the linewidths. These effects are not captured by changing the ρ–T relation, which only influences the thermal broadening.

Finally, spectrum S3 drawn from a single temperature model does not contain any regions significant to more than 10 per cent. Recall that this simulated spectrum has a large jump in optical depth, with mean fluxes $\bar{F} \sim 0.64$ and $\sim$0.60 for the first and second halves of the spectrum, respectively. This latter test demonstrates that the procedure of randomizing spectra works well – the original spectrum is equivalent to the randomized spectra for the statistic we investigate here. Note also that the method is not very sensitive to the mean effective optical depth. We apply the analysis procedure to data in the next Section.

5 THERMAL STATE OF THE IGM

5.1 Redshift range $z = 3, 3.6$

Two of our QSO spectra span the region around $z \sim 3.2$ where Schaye et al. (2000) claimed an increase in T_0. We have appended a stretch of spectrum of APM 0827+5255 to that of QSO 0302−003 and 0014+813, to have two more spectra that straddle the redshift $z \sim 3.2$. We use these spectra to investigate whether our new method independently suggests a change in T_0 around redshift $z \sim 3.2$. For each of the spectra, we have generated 200 randomized spectra to judge the significance of the temperature fluctuations as described earlier.

QSO 0055−269 does indeed appear to show a very sudden increase in T_0 around $z \sim 3.3$ (Fig. 12). Its low-redshift half is unusually hot at the 99.5 per cent level, and the high-redshift half is unusually cold at the 97 per cent level. It is worth noting that the low-redshift half contain two voids at $z \sim 3.11$ and 3.28 of sizes $\sim$17 and $15\,h^{-1}$ Mpc, respectively (deceleration parameter $q_0 = 0.1$; Kim et al. 2001b). This sudden transition looks very similar to what we had for our simulated spectrum S1 (but there the low-redshift half of S1 was cold). The identification of a statistically significant change in T_0 does not require the use of simulations. However, when we need to decide *by how much* T_0 changes, simulations are needed in order to calibrate the relation between the wavelet distribution and (T_0, γ).

QSO 1422+231 also shows an increase in T_0, albeit not so suddenly (Fig. 13). As for QSO 0055−269, the top (bottom) half is unusually cold (hot), at the 99.5 (97.5) per cent level. Note that there are large fluctuations in Δ in between the hot and cold regions, in the interval $z = [3.1, 3.4]$. In particular, it would be tempting to identify the hot region around $z \sim 3.37$ as being heated early, and/or the cold region around $z \sim 3.2$ as remaining cold slightly longer. However, the regions around $z \sim 3$ and $z \sim 3.5$ are much larger, hence far more significant. When randomized spectra are generated from this spectrum, many will actually contain large cold/hot regions as well, making the apparent fluctuations around $z \sim 3.2$ not statistically significant.

The combined spectrum of QSOs 0302−003 (from $z =$

[3, 3.27]) and APM 0827+5255 (from $z = [3.27, 3.7]$) is shown in Fig. 14. There is a sudden change in temperature at $z = 3.3$, with a significance of 100 per cent for the low-redshift hot half, and 99.5 per cent for the high-redshift colder region. QSO 0302−003 contains a well known void at $z \sim 3.17$ (Dobrzycki & Bechtold 1991) which is visible in Fig. 14 as a region of low absorption. We note that the higher-resolution data of Kim et al. (2001b) suggest a smaller size for the void than the earlier data. In any case, comparing the mean absorption with the temperature measure Δ, it is clear that the high inferred temperatures do *not* just result from the presence of these voids, although they might contribute to it.

The combined spectrum of QSOs 0014+813 (from $z = [3, 3.2]$) and APM 0827+5255 (from $z = [3.2, 3.7]$) is shown in Fig. 15. Below $z = 3.15$, this spectrum is hot at the 100 per cent level, above $z = 3.35$ it is cold at the 99.5 per cent level. In between, there are large-scale fluctuations similar to what we obtained for QSO 1422+231.

The probability of wavelet amplitudes, $P(A)$, is plotted in Fig. 16 for the unusual regions identified in these spectra. Consistent with the above evidence of a temperature jump, we find a change in shape of $P(A)$ around $z \sim 3.3$. Comparing the normalized distribution, $P(A/\langle A\rangle)$, with the simulations, we find good agreement between the high-redshift halves and the simulation with $(\log T_0, \gamma) = (4.18, 5/3)$, and the low-redshift half and the isothermal model $(\log T_0, \gamma) = (4.34, 1)$, respectively (Fig. 17). Using these values for γ, we can apply the calibration between $\langle A\rangle$ and $T_{1.2} \equiv T_0 1.2^{\gamma-1}$ from Fig. 10 to obtain an estimate for T_0. The result is in excellent agreement with the temperature evolution determined by Schaye et al. (2000) using the $b-N$ cut-off (Fig. 18). Above redshift $z \sim 3.4$, the temperature $T_0 \sim 10^{4.1\pm0.15}$; below that $T_0 \sim 10^{4.3\pm0.15}$, an increase of around 60 per cent.

We conclude that all four spectra show evidence for a change in temperature, significant at the ∼99 per cent level, over a relatively narrow redshift interval around $z \sim 3.3 \pm 0.2$. The temperature increase is 60 ± 14 per cent. Such an evolution is clearly not consistent with photoheating of a highly ionized, expanding medium, in which case the temperature would *smoothly decrease* towards lower z, but is consistent with a sudden entropy injection in the IGM resulting from He II reionization.

5.2 Redshift range $z = 2.6, 3.2$

We have combined the four intermediate redshift QSOs 0636+680, 0956+122, 0302−003 and 0014+813 into one longer spectrum, analysed in Fig. 19. The lowest redshift part of 0302 − 003 has a cold region of moderate significance ($P \sim 85$ per cent). In addition there is a hot region of size $\sim 10^4\,\mathrm{km\,s^{-1}}$ at a redshift $z \sim 3.1$ in the spectrum of 0014+813. This hot region is also significant if we analyse the spectrum of 0014+813 on its own (Fig. 20).

The wavelet amplitudes and the spectrum itself are compared for this peculiar region in the spectrum of QSO 0014+813 and two other stretches at comparable redshifts, in Fig. 21. What makes the spectrum in the top panel peculiar from the other two is that lines of comparable strength are broader and consequently produce smaller wavelet amplitudes. The analysis with 200 randomized spectra puts the statistical significance of the hot region at the $P = 99.5$ per cent level. Using the mean wavelet amplitude to estimate the temperature, we find that the difference in T_0 is 60 ± 30 per cent. This higher temperature is presumably a consequence of the region undergoing reionization later than the rest of the spectrum, although other processes might contribute as well.

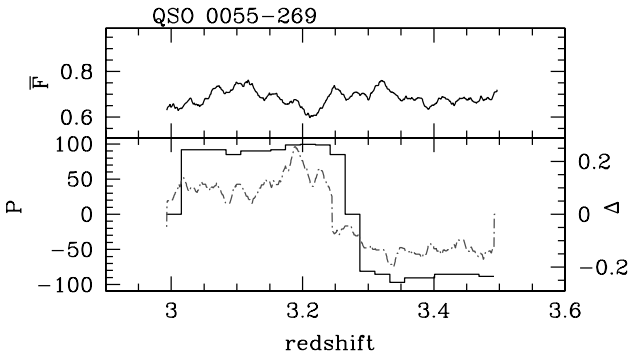

Figure 12. Wavelet analysis of the spectrum of QSO 0055− 269. Top panel: mean flux averaged over a window of $\partial v = 8000\,\mathrm{km\,s^{-1}}$. Bottom panel: temperature measure $\Delta(v, \partial v)$ (dot-dashed line, right-hand scale), and statistical significance $P(C_P)$, where C_P is defined in equation (5), of temperature fluctuations in per cent (histogram, left-hand scale). The low-redshift half of the spectrum is unusually hot at the 99.5 per cent level, and the high-redshift half of the spectrum is unusually cold at the 97 per cent level. The jump in temperature appears to be very sudden and occurs at a redshift $z \sim 3.3$. The mean absorption $\bar{F}$ does not appear to undergo a similar strong evolution.

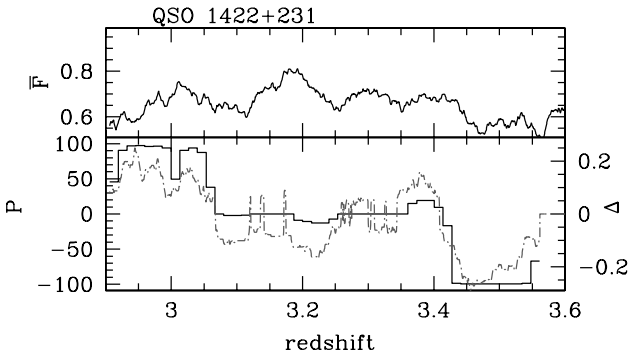

Figure 13. Same as Fig. 12 for QSO 1422+231, but for a window size of $\partial v = 5000\,\mathrm{km\,s^{-1}}$. Below $z \sim 3.05$, the spectrum is unusually hot at the 97.5 per cent level. Above $z \sim 3.4$ it is unusually cold at the 99.5 per cent level. In between, there appear to be large fluctuations in $\Delta(v, \partial v)$, which however are not statistically significant, when compared to the spectrum as a whole.

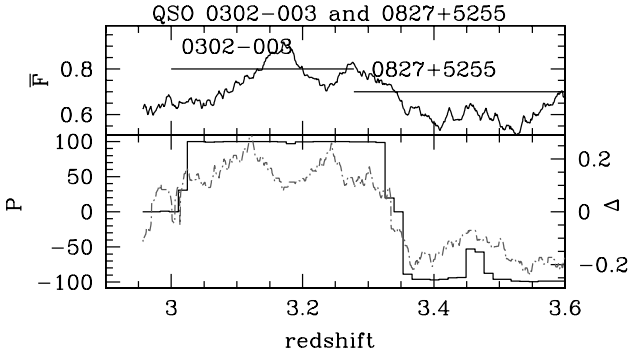

Figure 14. Same as Fig. 13 for QSO 0302− 003 (interval $z = [3, 3.27]$) and QSO APM 0827+5255 (interval $z = [3.27, 3.7]$). The spectrum below $z \sim 3.35$ is hot at the 100 per cent level, and above $z \sim 3.35$ it is cold at the 99.5 per cent level.

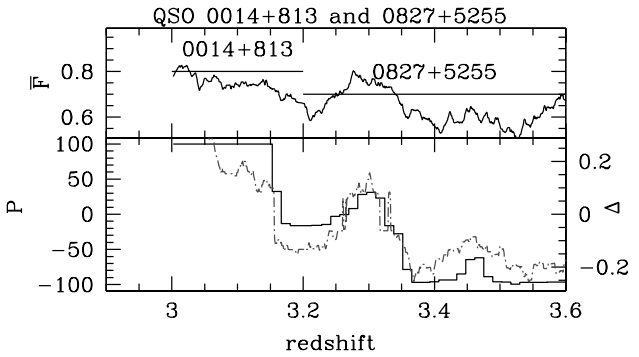

Figure 15. Same as Fig. 14 but for QSO 0014+813 (interval $z = [3, 3.2]$) and QSO APM 0827+5255 (interval $z = [3.2, 3.7]$). The spectrum below $z \sim 3.15$ is hot at the 100 per cent level, and above $z \sim 3.35$ it is cold at the 99.5 per cent level.

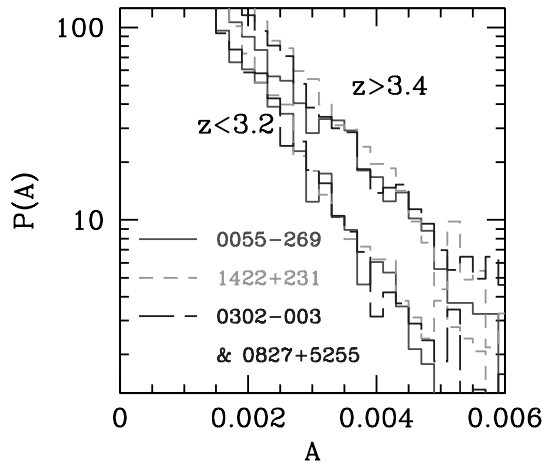

Figure 16. Probability distribution of wavelet amplitudes, $P(A)$, for the combined spectrum of QSOs 0302−003 and APM 0827+5255, and for QSOs 1422+231 and 0055−269. The high-redshift halves of the spectra ([3.37, 3.6], [3.45, 3.5] and [3.35, 3.5] respectively) and the low-redshift halves ([3.05, 3.3], [2.95, 3.05], [3.05, 3.25]) are shown separately. $P(A)$ for spectra at the same redshift are very similar, but there is a difference between the probability distributions at different redshifts.

5.3 Redshift range $z = 1.5, 2.4$

We have plotted the combined spectrum of the four low-redshift QSOs 0515−4414 ($z = [1.5, 1.7]$)], 2233−606 ($z = [1.8, 2.2]$), 1122−1648 ($z = [1.9, 2.4]$) and 2217−2818 ($z = [1.9, 2.3]$) in Fig. 22. QSO 2217−2818 contains a region of size $\sim 10^4\,\mathrm{km\,s^{-1}}$ [$\sim 100\,\mathrm{Mpc}\,h^{-1}$ comoving size in a $(\Omega_m, \Omega_\Lambda) = (0.3, 0.7)$ cosmology] which is colder at the 99 per cent significance level, when compared to 200 random realizations. The mean absorption does not appear to be unusual in this region. When analysing the spectrum of QSO 2217−2818 on its own, the cold region is equally significant at the 99.5 per cent level (Fig. 23).

The wavelet amplitudes and the spectrum itself are compared for this cold region and two other stretches at comparable redshifts in Fig. 24. The differences between the top panel and the two others is similar to what we found for the simulated spectrum S1 in Fig. 1, with the narrower lines in the top panel generating larger wavelet amplitudes. Using the mean wavelet amplitude to measure the temperature, we find the difference in T_0 is 77 ± 36 per cent.

At these lower redshifts, the number of metal lines, and the fraction of lines blended with metal lines, is no longer negligible.

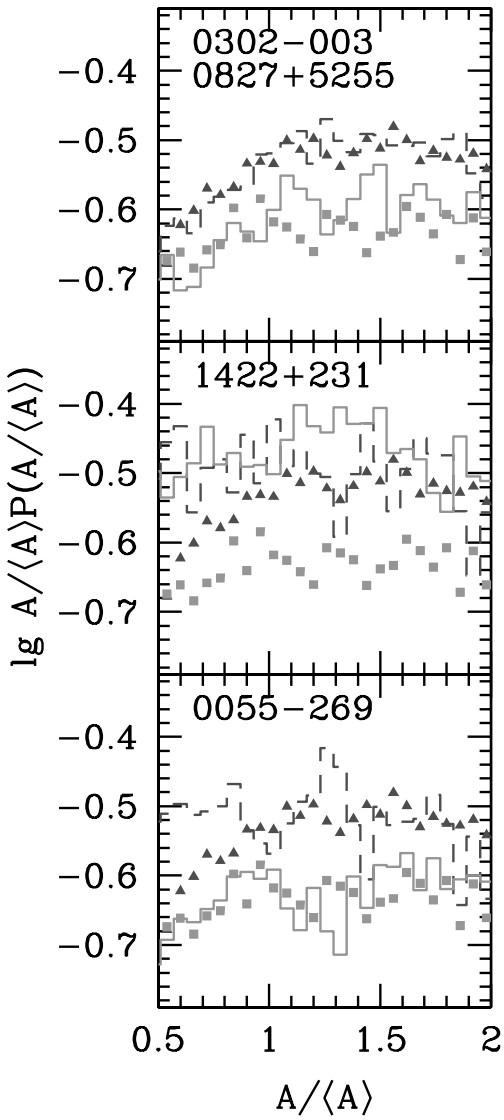

Figure 17. Same as Fig. 16, but for the distribution of wavelet amplitudes in units of the mean amplitude, $A/\langle A\rangle P(A/\langle A\rangle)$. Dashed lines refer to the high-redshift parts of the spectrum, full lines to the low-redshift halves. Filled triangles and filled squares refer to simulations with $(\log T_0, \gamma) = (4.18, 5/3)$ and (4.34,1), respectively. The high-redshift halves are well represented by the colder model with a steep $T-\rho$ relation, the lower-redshift halves are better fitted by the hotter, isothermal model.

In order to minimize the possibility that the detected cluster of narrow lines is significantly contaminated by such lines, two of us have independently fit the spectrum of QSO 2217−2818 using VPFIT. For each line not directly identified as a metal line, we have checked whether there is a consistent detection of Lyβ as well (the data are noisier at Lyγ, but we also demand consistency at that transition where possible, i.e. for $z > 2.137$). Unfortunately, metal transitions often have multiple components, and so if a transition were to be missed, it can contribute significantly to the signal. We have performed the wavelet analysis with these two independent line lists, and the results are nearly identical. Both detect an unusually large wavelet signal in the same region, at significance levels of 99.5 and 98.5 per cent, respectively.

From a theoretical point of view, if the temperature difference were due solely to a difference in reionization redshift, then a region could have an unusually low temperature if it had been

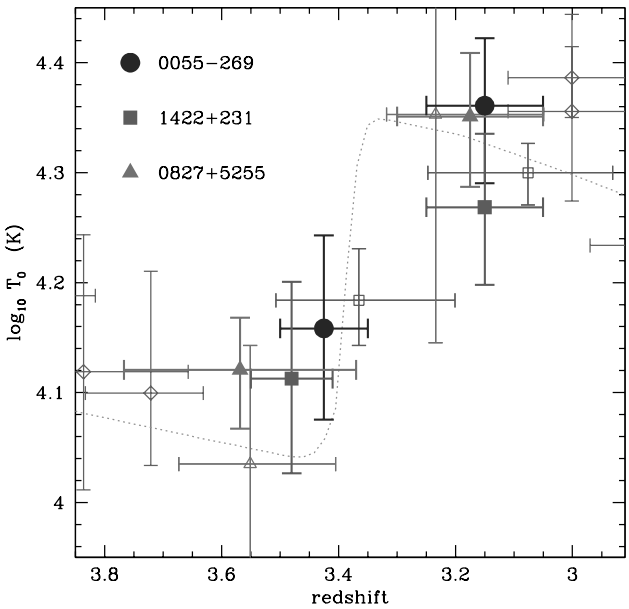

Figure 18. Temperature at the mean density, T_0, versus redshift. The open symbols with error bars are taken from Schaye et al. (2000). The filled symbols with error bars and thicker lines refer to estimates of T_0 based on the mean wavelet amplitudes and the calibration of Fig. 10, with errors on T_0 of 30 per cent for a stretch of spectrum of $5000\,\mathrm{km\,s^{-1}}$. Errors in the redshift direction refer to the redshift extent of the sampled region. Symbol types refer to the QSOs (note that APM 0827+5255 and 1422+231 were used in the analysis of Schaye et al. 2000 as well.) We have assumed $\gamma = 1$ below $z = 3.3$ and $\gamma = 5/3$ above $z = 3.3$ to convert $T_{1.2}$ to T_0. The dotted line shows the temperature evolution in a simulation where He II reionizes at redshift $\sim$3.4. It fits the data very well.

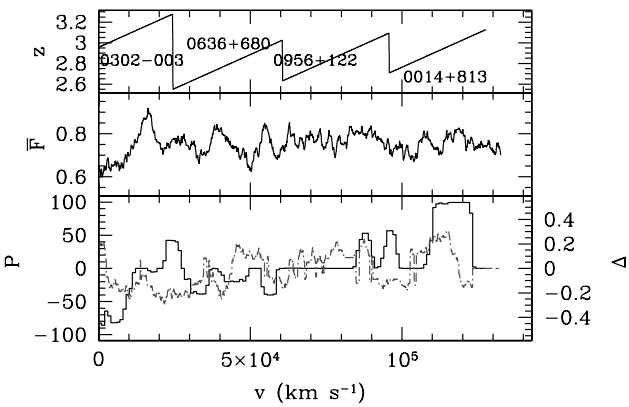

Figure 19. Combined spectrum of four $\bar{z} \sim 2.8$ QSOs as function of velocity v. Top panel: redshift range for each QSO; middle panel: mean flux averaged over $\partial v = 5 \times 10^3\,\mathrm{km\,s^{-1}}$; bottom panel: temperature indicator $\Delta(v, \partial v)$ (dot-dashed line, right-hand scale) and significance P in per cent (histogram, left-hand scale). There is a significantly hotter region ($P \sim 99$ per cent) of size $\sim 10^4\,\mathrm{km\,s^{-1}}$ at $v \sim 1.1 \times 10^5\,\mathrm{km\,s^{-1}}$ ($z \sim 3.0$) in the spectrum of QSO 0014+813.

reionized very early, or not at all. Assuming that $T \propto (1+z)^{1.8}$ after reionization, the early redshift would have to be $\sim$4.5. Both these possibilities seem unlikely to us. Given that we only detect one such unusual region over this redshift range, it seems more plausible that a combination of several effects, such as residual and partial contamination by metal lines, the presence of large-scale structure, and the gradual temperature decrease due to the

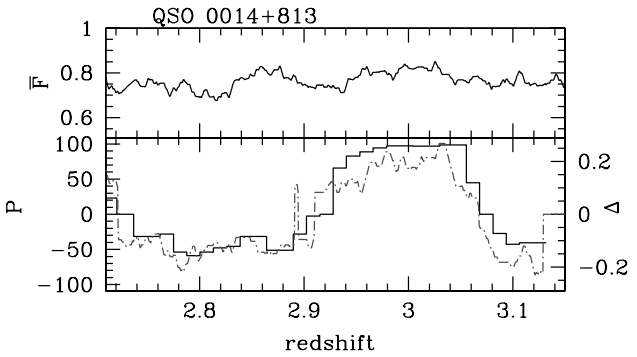

Figure 20. Same as Fig. 12, but for the spectrum of QSO 0014+813, using a window size $\partial v = 5000\,\mathrm{km\,s^{-1}}$. The hot region around $z \sim 3$ has a significance of 98.5 per cent.

expansion of the Universe, all contribute to making this region appear unusual. In addition, the voids in the spectrum at redshifts $z \sim 1.9$, 2.2 and 2.3 (Kim, Cristiani & D'Odorico 2001a) will contribute to the signal as well.

6 DISCUSSION

Schaye et al. (2000) determined the evolution of the ρ–T relation of the IGM by measuring the cut-off in the b–$N_{\rm HI}$ distribution of nine high-resolution QSOs. (Only two of those are in common with the ones used in the present analysis). They used high-resolution hydrodynamical simulations to calibrate the relation between the b–$N_{\rm HI}$ cut-off and the underlying ρ–T relation (Schaye et al. 1999). They inferred relatively high temperatures, $T_0 \sim 10^{4.1}$ K, $\gamma \sim 1.3$ at high redshifts $z = [4.5, 3.5]$, an apparently sharp rise to $T_0 \sim 10^{4.4}$ K around $z \sim 3$ with an associated dip in $\gamma \sim 1$, followed by a gradual decrease in T_0 and increase in γ towards $z \sim 2$. This temperature evolution is not consistent with photoheating in the optically thin limit, as determined from the Haardt & Madau (1996) tracks.

Ricotti et al. (2000) wrote down a partly theoretically motivated parametric function that describes the 2D distribution of lines in the b–$N_{\rm HI}$ plane. They employed dark matter simulations with an added 'pressure term' to mimic the effects of thermal smoothing, to calibrate the fitting parameters of the function, in terms of the simulation parameters. Their mock spectra were analysed with AUTOVP (Davé et al. 1997). Applying their method to published line lists, they obtained a thermal evolution consistent with that deduced by Schaye et al. (2000), although their error bars are large. In particular, they also stressed the small values of $\gamma \sim 1$ around $z \sim 3$.

Bryan & Machacek (2000) used high-resolution Eulerian simulations to measure T_0 from the b–$N_{\rm HI}$ cut-off. These authors stressed that the position of the cut-off also depends sensitively on the amplitude σ_8 of the underlying dark matter power spectrum. Bryan & Machacek used the Voigt profile fitter described in Zhang et al. (1997), which fits Gaussians to the *optical depth* distribution of absorption lines without attempting to deblend the absorption lines in terms of Voigt profiles, in contrast to VPFIT or AUTOVP. Theuns et al. (2000) showed that these other fitters appear much less sensitive to σ_8, which might partly explain the difference in σ_8 dependence. [Theuns & Zaroubi (2000) demonstrated that the wavelet analysis as described here is also not very sensitive to σ_8.] Bryan & Machacek inferred high temperatures as well, and also

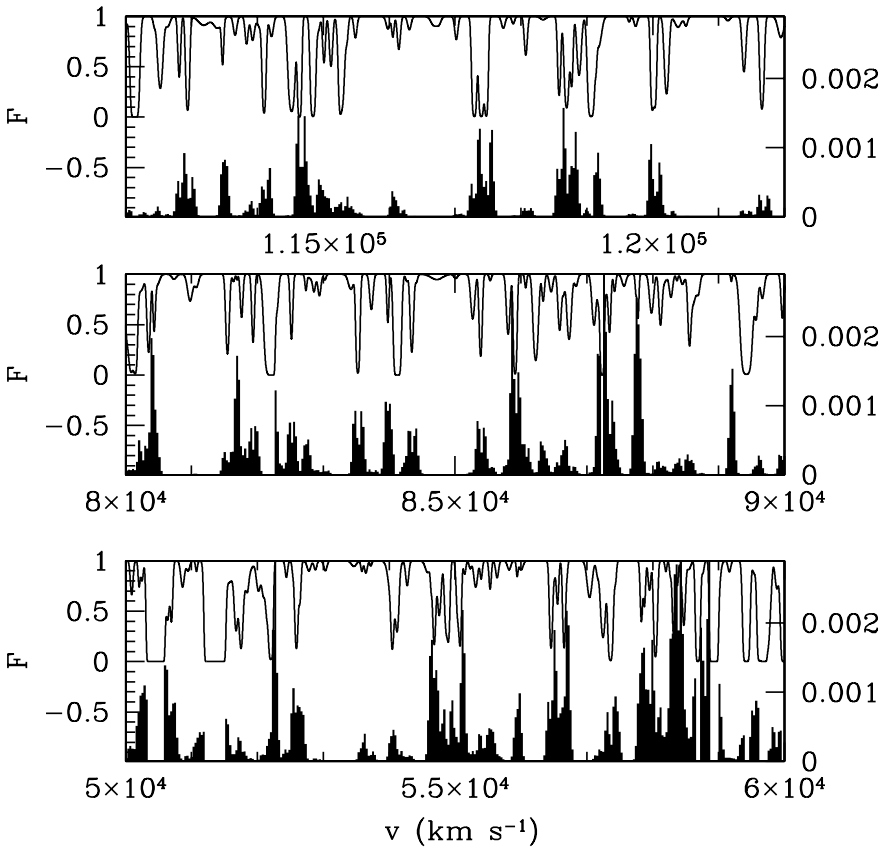

Figure 21. Flux (full lines, left-hand scale) and wavelet amplitudes (filled histograms, right-hand scales) for three regions of length $10^4\,\mathrm{km\,s^{-1}}$ taken from the spectrum shown in Fig. 19. The top panel corresponds to the hot region around $z \sim 3.1$ ($v \sim 1.1 \times 10^5\,\mathrm{km\,s^{-1}}$), the middle and bottom panels correspond to stretches of the spectrum at comparable redshifts which are not deemed unusual. Note the small fraction of narrow lines in the hot region, as compared to the other two.

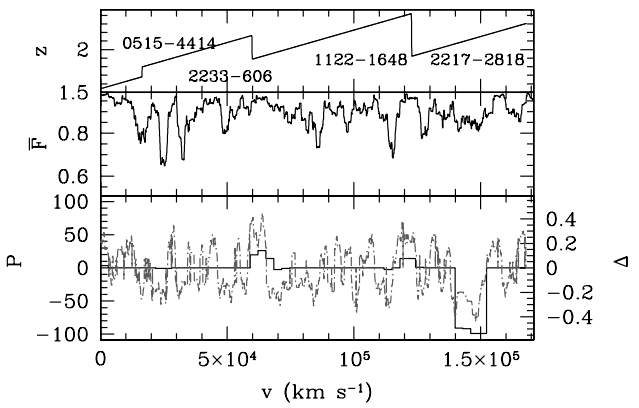

Figure 22. Combined spectrum of four $\bar{z} \sim 2$ QSOs as function of velocity v. Top panel: redshift range for each QSO; middle panel: mean flux averaged over $\partial v = 5 \times 10^3\,\mathrm{km\,s^{-1}}$; bottom panel: temperature indicator $\Delta(v, \partial v)$ (dot-dashed line, right-hand scale) and significance P in per cent (histogram, left-hand scale). There is a significantly colder region ($P \sim 99$ per cent) of size $\sim 10^4\,\mathrm{km\,s^{-1}}$ at $v \sim 1.5 \times 10^5\,\mathrm{km\,s^{-1}}$ ($z \sim 2$) in the spectrum of QSO 2217−2818.

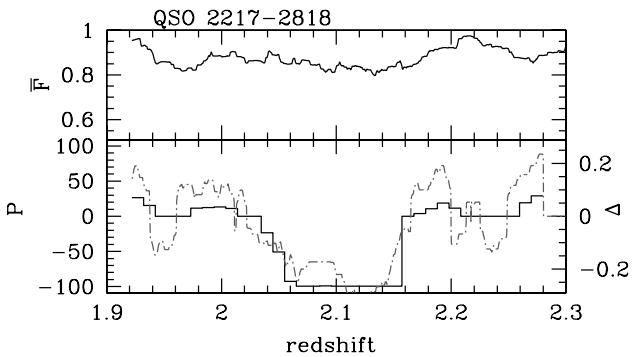

Figure 23. Same as Fig. 12 but for the spectrum of the low-redshift QSO 2217−2818, using a window size $\partial v = 5000\,\mathrm{km\,s^{-1}}$. The cold region in the middle of the spectrum has a significance of 99.5 per cent.

concluded that the heating by He II might be underestimated in the traditional models based on the optically thin limit.

McDonald et al. (2001) used a slightly different procedure to measure T_0 from the widths of the lines. They only use lines that are well-fitted by a single, unblended Voigt profile. T_0 is determined from the widths of those fits, correcting for other broadening contributions as a function of column density, using simulations. They find this correction to be large for low-density gas, and hence resort to measuring T_δ at an overdensity of $\delta \sim 1.5$. They find no evidence for evolution in $T_\delta \sim 10^{4.3}$ K with redshift, from $z \sim 3.9$ to 2.4. The redshift evolution of the temperature at a given overdensity, T_δ, depends on δ, because the photoheating rate depends on density (Miralda-Escudé & Rees 1994; see also fig. 3 in Schaye et al. 2000). It is not clear whether the measurement of $T_{1.5}$ by McDonald et al. (2001) is in contradiction with the

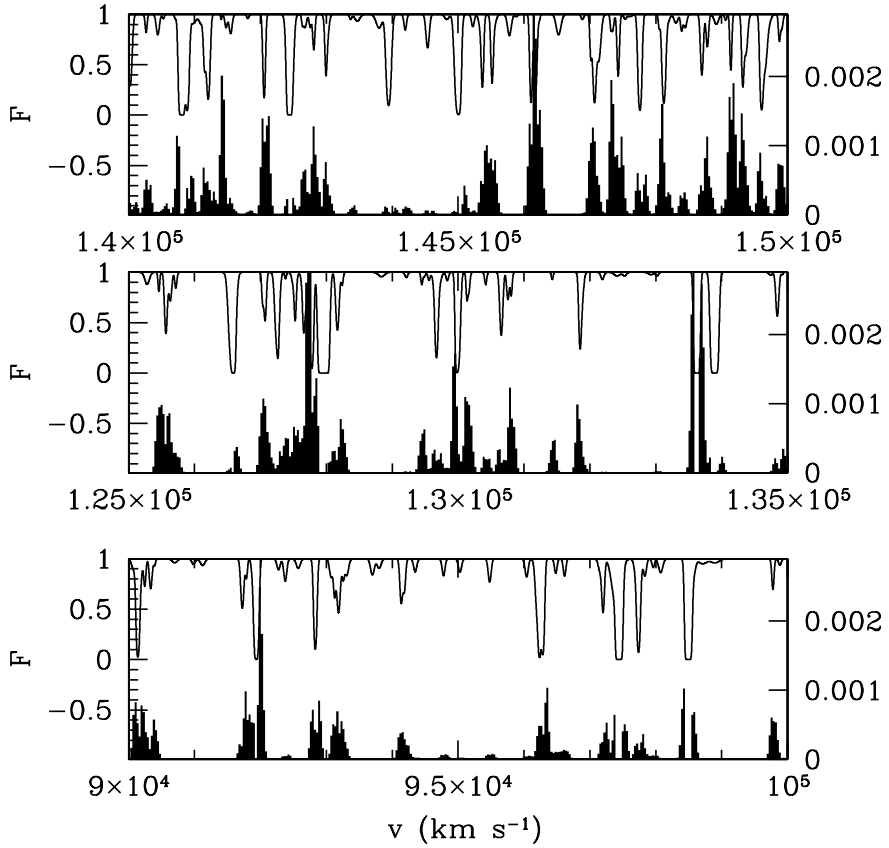

Figure 24. Flux (full lines, left-hand scale) and wavelet amplitudes (filled histograms, right-hand scales) for three regions of length $10^4\,\mathrm{km\,s^{-1}}$ taken from the spectrum shown in Fig. 22. The top panel corresponds to the cold region around $z \sim 2.1$ ($v \sim 1.5 \times 10^5\,\mathrm{km\,s^{-1}}$), the middle and bottom panels correspond to stretches of the spectrum at comparable redshifts which are not deemed unusual. Note the large fraction of narrow lines and the associated high wavelet amplitudes in the top panel. The two other panels do not contain such narrow lines.

determination of T_0 by the other groups, given the large uncertainty in γ quoted by all groups. The fact that their analysis is based on a single hydrodynamical simulation makes it difficult to judge the robustness of their analysis procedure. In addition, these authors averaged their results over wide redshift bins, which hampers their ability to detect sudden changes in T_0 or γ.

Zaldarriaga, Hui & Tegmark (2001) used the small-scale cut-off in the power spectrum as a measure of T_0. They find similar temperatures as McDonald et al. (2001), but unfortunately only use dark matter simulations to calibrate their results. Also Rollinde et al. (2001) use an inversion procedure to measure T_0 which is tested only on low-resolution dark matter simulations. Such simulations are inadequate to study the thermal properties of the IGM. Even simulations that include hydrodynamics need to be very accurate in order to resolve all the line broadening mechanisms properly (Theuns et al. 1998; Bryan et al. 1999). Therefore this type of analysis only shows that the method can deduce the temperature of the gas painted on top of a dark matter simulation using an untested prescription.

All determinations so far lead to higher values of T_0 than were expected for photoheating by a UV background dominated by QSOs, such as computed by Haardt & Madau (1996). One way to increase T_0 for a given UV background is to increase the baryon fraction $\omega_b \equiv \Omega_b h^2$, as the heating rate is proportional to the physical density of the gas (Miralda-Escudé & Rees 1994). Theuns et al. (1999) demonstrated that higher ω_b makes lines fitted by VPFIT considerably broader as T_0 increases. A higher value of ω_b would also allow galaxies to make a significant contribution to the UV background, as seems to be implied by the measurements of Steidel, Pettini & Adelberger (2001) of the large escape fraction of UV-photon from Lyman-break galaxies (Haehnelt et al. 2001). Without such a high ω_b, it would be difficult to explain the observed high opacity of the IGM. However, such high values of ω_b would appear to violate the tight constraints on $\omega_b \sim 0.0193 \pm 0.0014$ determined from the deuterium abundance (Burles & Tytler 1998; Kirkman et al. 2000).

Alternatively, higher values of T_0 can result from other heating mechanisms. The currently most popular one is that the calculations based on assuming an optically thin gas underestimate the photoheating rate, by a factor of up to a few (Miralda-Escudé & Rees 1994; Abel & Haehnelt 1999). Therefore, delayed He II reionization could be responsible for the increase in T_0 around $z \sim 3$, as suggested by Schaye et al. (2000), Ricotti et al. (2000) and Bryan & Machacek (2000). In fact, even the constant T_0 favoured by McDonald et al. (2001) requires an extra heating source, such as He II reionization.

If the sources responsible for reionizing He II are bright but scarce, then the temperature distribution could become quite inhomogeneous, with large He III regions separated from cooler, He II zones (Miralda-Escudé & Rees 1994). The ionizing radiation would quickly overrun the low-density voids, impulsively heating the gas, while the more overdense filamentary regions would remain neutral for longer (Miralda-Escudé, Haehnelt & Rees 2000). Because the lower-density gas then will be hotter, its neutral fraction would become even lower because of the $T^{-0.7}$ temperature dependence of the recombination coefficient. As a

result, the contrast in absorption between voids and filaments would increase even further.

The large jump in T_0 of 60 ± 14 per cent over the redshift interval $z = [3.5, 3.1]$ discussed in Section 5.1 strongly suggests a sudden entropy injection, likely resulting from He II reionization. Most of the wavelet signal comes from gas at modest overdensities $1 \lesssim \delta \lesssim 3$, which produces lines of column density $\sim 10^{13}\,\mathrm{cm}^{-1}$. This is because weaker lines do not contribute significantly to the wavelets, and stronger lines are both fewer and partly explicitly ignored in the analysis. This gas traces the modestly overdense filamentary pattern seen in simulations, and our analysis suggests it becomes reionized in He II in a fraction ~ 0.2 of a Hubble time. This also naturally explains the relatively high values of T_0 found at lower redshifts.

A sudden increase in T_0 influences the gas distribution in shallow potential wells. Theuns et al. (2000) explicitly showed how increased heating can drive gas out of the centers of filaments into the lower density surroundings. The velocity of this gas also contributes to the linewidths as determined by Voigt-profile fitting. Such impulsive heating may influence the formation of haloes of virial temperatures $\lesssim 2. \times 10^4$ K (Gnedin 2000b).

After reionization, the IGM temperature will fall at a rate $T_0 \approx (1+z)^{1.8}$, slower than pure adiabatic expansion because of the continuing photoheating. Over a redshift extent $\delta z \sim 0.5$ of the Lyα forest of a QSO, this corresponds to a drop of ~ 27 and 32 per cent at redshifts 3 and 2.5, respectively, between the high- and low-redshift parts of the QSOs spectrum. This will contribute to making the top half of QSO 0014+813 unusually hot, and the bottom half of QSO 2217−2818 unusually cold. Similarly, if He II reionization were delayed in one region with respect to another, for example as a result of QSO clustering, then we might expect to see differences in T_0 of order 40 per cent, given our estimate of $z = 3.3 \pm 0.15$ for the duration of the reionization epoch. Such entropy fluctuations are likely to remain present for a long time afterwards, given that the IGM evolves nearly isentropically after reionization.

Why don't we see fluctuations on smaller scales? The analysis of spectrum S2 suggests that the present method can detect fluctuations of amplitude 50 per cent in T_0 on scales as small as $5 \times 10^3\,\mathrm{km\,s}^{-1}$. However, our simulations are clearly somewhat idealized: they lack large-scale power, and in addition have an imposed ρ–T relation *without any* scatter. In the real Universe, the presence of large-scale power and scatter in the ρ–T will tend to increase the intrinsic fluctuations in the wavelet amplitudes, making it harder to recognize a stretch of spectrum with truly different T_0 or γ. This is particularly true around reionization, where small-scale fluctuations would be hard to detect in the presence of a large jump in the spectrum as a whole. However, the absence of small-scale fluctuations away from reionization suggests that the IGM does obey a reasonably well defined T–ρ relation on sufficiently large scales $\geqslant 5000\,\mathrm{km\,s}^{-1}$. Given the arguments above it also suggest that reionization occurred relatively well synchronized throughout the IGM.

7 SUMMARY

We have presented a method that uses wavelets to characterize objectively the linewidths of Lyα lines in a QSO spectrum. Colder gas produces narrower absorption lines, for which the wavelet amplitudes are larger. We described a statistical method, based on recognizing regions where the distribution of wavelet amplitudes is unusual, to identify regions where the temperature at the mean density, T_0, differs significantly from the mean. The significance level is determined by performing the wavelet analysis on spectra obtained from the data after scrambling the list of absorption lines, thereby destroying all correlations imprinted by (temperature) fluctuations.

We applied this method to mock spectra generated from high-resolution hydrodynamical simulations. We imposed several ρ–T relations on the output from these simulations, and used them to construct spectra with intrinsic temperature fluctuations. We demonstrated that the method is able to detect fluctuations in T_0 of ~ 50 per cent in regions as small as $5000\,\mathrm{km\,s}^{-1}$ at redshift $z = 3$, at the 95 per cent level. We also showed that by calibrating the relation between the average wavelet amplitude, $\langle A \rangle$, and T_0 using our hydrodynamical simulations, one can estimate the IGM temperature with an rms error of the order of 30 per cent, per stretch of spectrum of $5000\,\mathrm{km\,s}^{-1}$.

We have applied the method to 11 high-resolution QSO spectra. There is strong evidence of a sharp *increase* in T_0 by a factor $\sim 60 \pm 14$ per cent over the redshift interval $z = [3.5, 3.1]$. We interpreted this as evidence for He II reionization, and concluded that it took of the order of $\delta z \sim 0.4$ to reionize the filaments at overdensity ~ 3, which our method is most sensitive to. Our estimate for the temperatures above and below the jump are $T_0 \approx 10^{4.1 \pm 0.15}$ and $T_0 \sim 10^{4.3 \pm 0.15}$ K, respectively. These values are in excellent agreement with those obtained by Schaye et al. (2000), who used a very different method.

At lower redshifts, we find that the IGM appears to follow a reasonably well defined T–ρ relation on scales larger than $5000\,\mathrm{km\,s}^{-1}$. In eight QSO spectra, we only found two unusual regions, significant at the more than 99 per cent level. QSO 0014+813 has a hot region of size $10^4\,\mathrm{km\,s}^{-1}$ at $z \sim 3.1$, where the temperature is around 60 ± 30 per cent higher. This could be a relic of He II reionization, enhanced by the overall decrease in T_0 along the spectrum as a result of adiabatic expansion. QSO 2217−2818 has a cold region of similar size, at $z \sim 2.3$, where T_0 is lower by $\sim 77 \pm 36$ per cent. Again in addition to adiabatic expansion, the three voids in this spectrum will contribute to making this region unusual.

ACKNOWLEDGMENTS

The data presented herein were obtained at the W. M. Keck Observatory, which is operated as a scientific partnership among the California Institute of Technology, the University of California and the National Aeronautics and Space Administration. The Observatory was made possible by the generous financial support of the W. M. Keck foundation. This paper is based on public data released from the VLT/UVES Commissioning and Science Verification and from the OPC porgramme 65.O-296A (PI S.-D'Odorico) at the VLT/Kueyen telescope, ESO, Paranal, Chile. We would like to thank Joop Schaye for a careful reading of the paper, and many stimulating discussions. We are also grateful to S. D'Odorico, S. Cristiani, E. Giallongo, A. Fontana and S. Savaglio for allowing us to use the line list of Q0055−269 prior to publication. TT thanks PPARC for the award of an Advanced Fellowship. This work has been supported by the 'Formation and Evolution of Galaxies' and 'Physics of the Intergalactic Medium' networks set up by the European Commission. Research was conducted in cooperation with Silicon Graphics/Cray Research utilising the Origin 2000 supercomputer at DAMTP, Cambridge.

REFERENCES

Abel T., Haehnelt M. G., 1999, ApJ, 520, L13
Bahcall J. N., Salpeter E. E., 1965, ApJ, 142, 1677
Bi H. G., Boerner G., Chu Y., 1992, A&A, 266, 1
Bi H., Davidsen A. F., 1997, ApJ, 479, 523
Boksenberg A., Sargent L. W. L., Rauch M., 1998, preprint (astro-ph/9906459)
Bryan G. L., Machacek M., Anninos P., Norman M. L., 1999, ApJ, 517, 13
Bryan G. L., Machacek M. E., 2000, ApJ, 534, 57
Burles S., Tytler D., 1998, ApJ, 507, 732
Carswell R. F., Webb J. K., Baldwin J. A., Atwood B., 1987, ApJ, 319, 709
Cen R., Miralda-Escudé J., Ostriker J. P., Rauch M., 1994, ApJ, 437, L9
Couchman H. M. P., 1991, ApJ, 368, L23
Couchman H. M. P., Thomas P. A., Pearce F. R., 1995, ApJ, 452, 797
Davidsen A. F., Kriss G. A., Wei Z., 1996, Nat, 380, 47
Davé R., Hernquist L., Weinberg D. H., Katz N., 1997, ApJ, 477, 21
Daubechies I., 1988, Commun. Pure Appl. Math., 41, 909
Dobrzycki A., Bechtold J., 1991, ApJ, 377, L69
D'Odorico S. et al., 2000, SPIE Proc., 4005, 121
Efstathiou G., Schaye J., Theuns T., 2000, Roy. Soc. Lond. Phil. Trans. Ser., 358, 2049
Ellison S. L., Lewis G. F., Pettini M., Sargent W. L. W., Chaffee F. H., Foltz C. B., Rauch M., Irwin M. J., 1999, PASP, 111, 946
Fontana A., Ballester P., 1995, The ESO Messenger, 80, 37
Gingold R. A., Monaghan J. J., 1977, MNRAS, 181, 375
Giroux M. L., Shull J. M., 1997, AJ, 113, 1505
Gnedin N. Y., 2000a, ApJ, 535, 530
Gnedin N. Y., 2000b, ApJ, 542, 535
Gunn J. E., Peterson B. A., 1965, ApJ, 142, 1633
Haardt F., Madau P., 1996, ApJ, 461, 20
Haehnelt M. G., Madau P., Kudritzki R., Haardt F., 2001, ApJ, 549, L151
Heap S. R., Williger G. M., Smette A., Hubeny I., Sahu M. S., Jenkins E. B., Tripp T. M., Winkler J. N., 2000, ApJ, 534, 69
Hernquist L., Katz N., Weinberg D. H., Miralda-Escudé J., 1996, ApJ, 457, L51
Hu E. M., Kim T.-S., Cowie L. L., Songaila A., Rauch M., 1995, AJ, 110, 1526
Hui L., Gnedin N. Y., 1997, MNRAS, 292, 27
Irwin M. J., Ibata R. A., Lewis G. F., Totten E. J., 1998, ApJ, 505, 529
Jamkhedar P., Bi H., Fang L., 2001, ApJ, 561, 94
Kim T.-S., Cristiani S., D'Odorico S., 2001a, A&A, 373, 757
Kim T.-S., Carswell R. F., Cristiani S., D'Odorico S., Giallongo E., 2001b, preprint
Kirkman D., Tytler D., 1997, ApJ, 484, 672
Kirkman D., Tytler D., Burles S., Lubin D., O'Meara J. M., 2000, ApJ, 529, 655
Lucy L. B., 1977, AJ, 82, 1023
Machacek M. E., Bryan G. L., Meiksin A., Anninos P., Thayer D., Norman M., Zhang Y., 2000, ApJ, 532, 118
McDonald P., Miralda-Éscude J., Rauch M., Sargent W. L. W., Barlow T. A., Cen R., 2001, ApJ, 562, 52
Meiksin A., 2000, MNRAS, 314, 566
Miralda-Escudé J., Cen R., Ostriker J. P., Rauch M., 1996, ApJ, 471, 582
Miralda-Escude J., Rees M. J., 1994, MNRAS, 266, 343
Miralda-Escudé J., Haehnelt M., Rees M. J., 2000, ApJ, 530, 1
Pando J., Fang L. Z., 1996, ApJ, 459, 1
Press W. H., Teukolsky S. A., Vetterling W. T., Flannery B. P., 1992, Numerical Recipes. Cambridge University Press
Rauch M., 1998, ARA&A, 36, 267
Rauch M. et al., 1997, ApJ, 489, 7
Reimers D., Kohler S., Wisotzki L., Groote D., Rodriguez-Pascual P., Wamsteker W., 1997, A&A, 327, 890
Ricotti M., Gnedin N. Y., Shull J. M., 2000, ApJ, 534, 41
Rollinde E., Petitjean P., Pichon C., 2001, MNRAS, 326, 597
Schaye J., 2001, ApJ, 559, 507
Schaye J., Theuns T., Leonard A., Efstathiou G., 1999, MNRAS, 310, 57
Schaye J., Theuns T., Rauch M., Efstathiou G., Sargent W. L. W., 2000, MNRAS, 318, 817
Seljak U., Zaldarriaga M., 1996, ApJ, 469, 437
Songaila A., 1998, AJ, 115, 2184
Songaila A., Cowie L. L., 1996, AJ, 112, 335
Steidel C. C., Pettini M., Adelberger K. L., 2001, ApJ, 546, 665
Theuns T., Zaroubi S., 2000, MNRAS, 317, 989
Theuns T., Leonard A., Efstathiou G., Pearce F. R., Thomas P. A., 1998, MNRAS, 301, 478
Theuns T., Leonard A., Schaye J., Efstathiou G., 1999, MNRAS, 303, L58
Theuns T., Schaye J., Haehnelt M. G., 2000, MNRAS, 315, 600
Vogt S. S. et al., 1994, SPIE Proc., 2198, 362
Wadsley J., Bond J. R., 1996, in Clarke D., West M., eds, Proc. 12th Kingston Conf., Computational Astrophysics. Astron. Soc. Pac., San Francisco
Webb J. K., 1987, PhD thesis, Univ. Cambridge
Zaldarriaga M., 2002, ApJ, 564, 153
Zaldarriaga M., Hui L., Tegmark M., 2001, ApJ, 557, 519
Zhang Y., Anninos P., Norman M. L., 1995, ApJ, 453, L57
Zhang Y., Anninos P., Norman M. L., Meiksin A., 1997, ApJ, 485, 496

This paper has been typeset from a TEX/LATEX file prepared by the author.